Reviews in Mineralogy & Geochemistry
Vol. 71 pp. 169-199, 2010

Spin-State Crossover of Iron in Lower-Mantle Minerals: Results of DFT+*U* Investigations

Han Hsu

Department of Chemical Engineering and Materials Science
University of Minnesota
Minneapolis, Minnesota 55455-0132, U.S.A.

hsuhan@cems.umn.edu

Koichiro Umemoto

Department of Geology and Geophysics
University of Minnesota,
Minneapolis, Minnesota 55455-0132, U.S.A.

umemoto@cems.umn.edu

Zhongqing Wu

Department of Physics
University of South California
Los Angeles, California 90007, U.S.A.

zhongwu@usc.edu

Renata M. Wentzcovitch

Department of Chemical Engineering and Materials Science
University of Minnesota
Minneapolis, Minnesota 55455-0132, U.S.A.

wentzcov@cems.umn.edu

INTRODUCTION

The lower mantle is the largest layer of the Earth. Pressures and temperatures there vary from 23 GPa to 135 GPa and ~1,900 K to 4,000 K. Aluminous perovskite, Al-$Mg_{1-x}Fe_xSiO_3$, and ferropericlase, $Mg_{1-x}Fe_xO$, are the most important phases of the Earth's lower mantle, comprising ~62 vol% and ~35 vol% of this region, respectively. The remaining consists of $CaSiO_3$-perovskite, according to the pyrolitic compositional model (Ringwood 1982). Silicate perovskite transforms into another polymorph, post-perovskite, at conditions expected to occur near the D″ discontinuity in the deep slower mantle, i.e., 2,500 K and 125 GPa (Murakami et al. 2004; Oganov and Ono 2004; Tsuchiya et al. 2004; Wentzcovitch et al. 2006). The spin-state crossover (also referred to as "spin pairing transition" or "spin(-state) transition") of iron in ferropericlase under pressure was observed in 2003 by X-ray emission spectroscopy (XES) (Badro et al. 2003). In the following year a similar phenomenon was also identified in iron-bearing perovskite ($Mg_{1-x}Fe_xSiO_3$) by the same technique (Badro et al. 2004). This phenomenon had been predicted for decades (Fyfe 1960; Gaffney and Anderson 1973; Ohnishi 1978; Sherman 1988, 1991; Sherman and Jansen 1995; Cohen et al. 1997) but the pressure conditions were challenging for this type of experiment and it took several decades to observe it. The implications of this phenomenon for the properties of this region, or of the entire planet, are yet to be understood. Today, theoretical studies are

1529-6466/10/0071-0009$05.00 DOI: 10.2138/rmg.2010.71.09

making decisive contributions to this problem. This article reviews the main theoretical results on the spin-state crossover in the lower mantle phases.

Spin changes in strongly correlated oxides and silicates under pressure is the type of problem that has challenged electronic structure theory for decades. Ferrous (Fe^{2+}) and ferric (Fe^{3+}) irons are strongly correlated ions. The established first principles framework used to describe electronic states in solids, density functional theory (DFT) (Hohenberg and Kohn 1964; Kohn and Sham 1965), has not so far been able to explain some of the most fundamental properties of materials containing these ions: whether they are insulators or metals. For decades this challenge has inspired the development of new methods for electronic structure computations that may be reaching maturity just in time to address this problem. In this paper, we offer a review of theoretical/computational studies that have been performed to date on these two materials and analyze the performance of different approaches by contrasting results with each other and with experimental measurements. We also emphasize the geophysical implications of these results when possible. The results summarized here were obtained using standard DFT within the local density approximation (LDA) (Ceperley and Alder 1980; Perdew and Zunger 1981), the generalized gradient approximation (GGA) (Perdew et al. 1996), or the internally consistent DFT+U approach (Cococcioni and de Gironcoli 2005; Cococcioni et al. 2010). DFT, with its various approximations to exchange-correlation energy, is reviewed in this volume (Perdew and Ruzsinszky 2010; Zhao and Truhlar 2010). The DFT+U method (see Cococcioni 2010) is sufficiently developed to the point that can address structurally complex strongly correlated minerals. For a general review of the spin crossover in ferropericlase and perovskite, including experiments up to 2007-08, we refer to a recent paper, Lin and Tsuchiya (2008). Experimental information that has become available since the publication of this review and that is relevant for comparison with calculations is reviewed here.

THE SPIN-PAIRING PHENOMENON

The 5-fold degeneracy of the 3*d* atomic states of iron splits in a crystalline field. The nature and ordering of the new energy levels depend primarily on the atomic arrangement of the neighboring ions and their distances. A comprehensive study of the electronic states of transition metal ions in crystalline fields can be found in the book by Sugano et al. (1970). The electronic states of iron in Earth's forming silicates and oxides at ambient conditions are relatively localized. In stoichiometric compounds such as FeO, Fe_2O_3, etc., the magnetic moments of iron are usually ordered anti-ferromagnetically. The solid solutions of the lower mantle are not magnetically ordered. In ferropericlase and iron-bearing perovskite, the energetic order, symmetry, and occupation of the 3*d* orbitals of iron can be understood on the basis of crystal field symmetry and Hunds rule. Ferrous iron has six 3*d* electrons. In the high-spin (HS) state, five of them have spin +1/2 (up) and one has spin −1/2 (down). Their angular momentum is essentially quenched, spin orbit interaction is practically non-existent, and the total-spin quantum number, S, is equal to 2. The intermediate-spin (IS) state has four 3*d* electrons with spin up and two with spin down, for a total spin $S = 1$. The low-spin (LS) state, has three electrons up, three down, and $S = 0$. Ferric iron has five 3*d* electrons; the HS state has five spin up electrons, for $S = 5/2$; the IS and LS states have $S = 3/2$ and 1/2 respectively. The charge density distribution of the partially occupied 3*d* electrons is non-spherical and is related to the ordering of the energy levels established by the crystalline field and the number of 3*d* electrons. This non-spherical distribution distorts the first coordination shell of ligands, the so-called Jahn-Teller (J-T) effect.

In the Earth forming minerals we will review, iron is in the HS state at zero pressure. Under pressure, the Fe-O bond-length decreases, the crystal field increases, and the energy splitting between the *d*-orbital derived states increases. This leads to a change in the occupation of these orbitals, i.e., the spin pairing phenomenon characterized by a change in the occupation of the lowest lying *d*-orbitals and a change in the total spin S. How these occupations change under pressure is not obvious. In principle, spins could pair gradually, with a change of S from 2 to 1 to 0 in ferrous iron and from 5/2 to 3/2 to 1/2 in ferric iron. In fact, it depends on unpredictable factors (e.g., chemistry, stoichiometry, etc.) and it is often difficult to anticipate or explain the nature of these spin changes. For instance, spin changes in (Mg,Fe)SiO_3-perovskite is a current topic of controversy.

One should have in mind that in the Hubbard model, usually invoked to describe the electronic structure of these solids, it is the ratio U/Δ, where U is the Coulomb correlation energy and Δ is the *d*-bandwidth, that characterizes the correlation strength, with $U/\Delta >> 1$ ($U/\Delta << 1$) corresponding to the strong (weak) correlation limit. Under pressure the band width Δ increases and the strength of the correlation decreases.

THEORETICAL APPROACH

The spin crossover systems we will review are paramagnetic solid solutions, insulators with localized moments on the iron site. Besides, the iron concentration, X_{Fe}, is relatively low ($X_{Fe} < 0.2$). There are a few challenges in addressing properties of these systems: description of their electronic structure, treatment of the solid solution problem, and calculation of their vibrational properties, without which no thermodynamics treatment is possible. The methods chosen to address these issues are outlined below.

Spin- and volume-dependent Hubbard *U*

The strongly correlated behavior of iron in the oxides and silicates of the mantle has deterred the use of standard DFT for predictive studies. DFT results are particularly poor for ferropericlase, which is predicted to be metallic with DFT, rather than insulator (Tsuchiya et al. 2006). The corrections for the electron-electron interaction on the iron sites can be included by using the so-called DFT+U method. Here we used a rotationally invariant version of the DFT+U approach implemented in the plane wave pseudopotential method, where U is calculated in an internally consistent way (Cococcioni and de Gironcoli 2005). Details of this method are also discussed by Cococcioni (2010) in this volume. In short, the total energy functional in the DFT+U is:

$$E_{DFT+U} = E_{DFT} + \frac{U}{2}\sum_{I,\sigma} Tr\left[\mathbf{n}^{I\sigma}\left(\mathbf{1}-\mathbf{n}^{I\sigma}\right)\right] \tag{1}$$

where E_{DFT} is the DFT ground-state energy of the structure, and $\mathbf{n}^{I\sigma}$ is the occupation matrix of the atomic site I with spin σ. The atomic-like orbitals used in defining $\mathbf{n}^{I\sigma}$ are arbitrary, but the calculations of U and E are consistent with this definition (Cococcioni and de Gironcoli 2005; Fabris et al. 2005). The Hubbard U is computed using linear response theory. In practice this procedure starts by computing the DFT ground state of a given structure. The occupation matrix $\mathbf{n}^{I\sigma}$ at site I is determined from the DFT ground state. The next step is to apply perturbations to the potential localized at the Hubbard site I. The perturbed states lead to different occupation matrices. The linear response of the occupation matrix $\mathbf{n}^{I\sigma}$ to the local potential shift is used to determine the Hubbard U. In this scheme, the value of U depends on both the spin state and the unit-cell volume (Cococcioni and de Gironcoli 2005; Tsuchiya et al. 2006; Hsu et al. 2009a).

The calculation of pressure in the DFT+U method presents an issue that is pervasive in this method: the calculation of gradients. Since U depends on volume, the pressure P determined by the negative derivative of the total energy E_{DFT+U} (see Eqn. 1) with respect to volume V has the following form:

$$P = -\frac{\partial E_{DFT}}{\partial V} - \frac{U}{2}\sum_{I,\sigma}\frac{\partial}{\partial V} Tr\left[\mathbf{n}^{I\sigma}\left(\mathbf{1}-\mathbf{n}^{I\sigma}\right)\right] - \frac{\partial U}{2\partial V}\sum_{I,\sigma} Tr\left[\mathbf{n}^{I\sigma}\left(\mathbf{1}-\mathbf{n}^{I\sigma}\right)\right] \tag{2}$$

The first two terms are obtained from a modified form of the first principles stress (Nielsen and Martin 1983) in a plane wave basis set. However, pressure depends also on the volume dependence of U (last term in Eqn. 2), which is not obtained *a priori*. The same problem arises in the calculation of other structural gradients. U should be structurally consistent and currently its gradient with respect to positions, strains, etc, is not calculated. Nevertheless, the first two terms in Equation (2) are calculated and they can be used to move atoms, in the case of forces, or change volume, in the case of stress/pressure, after which U can be recomputed until the structural degrees of freedom and U converge. Pressure and other structural gradients in this method are currently calculated numerically by finite differences from E_{DFT+U}, with structurally consistent U (Hsu et al. 2009a).

It should be mentioned that the Hubbard U can be determined more rigorously by perturbing the ground state of a series of DFT+U ground state with several chosen input Us. In this approach, the consistency between the response and the DFT+U ground states should be achieved. The Hubbard U determined this way is called self-consistent U (Kulik et al. 2006). This method, however, was not used in calculations reviewed here.

Thermodynamic treatment of the mixed spin state

At finite temperatures, ferropericlase or perovskite with iron concentration X_{Fe} can have irons in multiple spin states, i.e., in a mixed-spin (MS) state. Knowledge of the equilibrium population of each spin state at any given temperature and pressure is crucial to study the consequences of the spin crossover on their properties. Since X_{Fe} of these minerals in actual lower mantle are relatively small (~0.18 and ~0.12 for ferropericlase and perovskite respectively), we treat the ferropericlase and perovskite in the MS state as the ideal solid solution of the mixture of each pure spin state. (NOTE: this is not the same as a solid solution of MgO and FeO). The Gibbs free energy of the MS state is thus written as

$$G(n_\sigma,P,T)=\sum_\sigma n_\sigma(P,T)G_\sigma(P,T)+G^{mix}(P,T) \tag{3}$$

where n_σ and G_σ are the fraction and Gibbs free energy of each spin state, respectively. The subscript σ denotes spin state, i.e., LS, IS, HS, etc. The term G^{mix} results from the entropy of mixing solution, and it is given by

$$G^{mix}=k_BTX_{Fe}\sum_\sigma n_\sigma \log n_\sigma \tag{4}$$

The Gibbs free energy of each spin state G_σ has three contributions:

$$G_\sigma=G_\sigma^{stat+vib}+G_\sigma^{mag}+G_\sigma^{site} \tag{5}$$

where $G_\sigma^{stat+vib}$ is the Gibbs free energy containing static and vibrational contributions. The calculation of the vibrational free energy will be addressed in the next subsection. If this contribution is disregarded, $G_\sigma^{stat+vib}$ reduces to the static enthalpy of spin state σ,

$$G_\sigma^{stat+vib}=H_\sigma \tag{6}$$

The second term in Equation (5) derives from the magnetic entropy,

$$G_\sigma^{mag}=-k_BTX_{Fe}\log\left[m_\sigma(2S_\sigma+1)\right] \tag{7}$$

where m_σ and S_σ are the orbital degeneracy and the spin quantum number of each spin state, respectively. The third term comes from the site entropy

$$G_\sigma^{site}=-k_BTX_{Fe}\log N_\sigma^{site} \tag{8}$$

where N_σ^{site} is the number of equivalent equilibrium sites for irons in each spin state.

By minimizing the total Gibbs free energy (Eqn. 3) with respect to n_σ under the constraint

$$\sum_\sigma n_\sigma = 1 \tag{9}$$

the following expressions for each spin state are then obtained:

$$n_\sigma(P,T) = n_{HS} \times \frac{N_\sigma^{site} m_\sigma (2S_\sigma + 1)}{N_{HS}^{site} m_{HS}(2S_{HS}+1)} \exp\left(-\frac{\Delta G_\sigma^{stat+vib}}{k_B T X_{Fe}}\right) \quad \text{for } \sigma \neq \text{HS}$$

$$n_{HS}(P,T) = \left[1 + \frac{N_{LS}^{site} m_{LS}(2S_{LS}+1)}{N_{HS}^{site} m_{HS}(2S_{HS}+1)} \exp\left(-\frac{\Delta G_{LS}^{stat+vib}}{k_B T X_{Fe}}\right) + \frac{N_{IS}^{site} m_{IS}(2S_{IS}+1)}{N_{HS}^{site} m_{HS}(2S_{HS}+1)} \exp\left(-\frac{\Delta G_{IS}^{stat+vib}}{k_B T X_{Fe}}\right)\right]^{-1} \tag{10}$$

where $\Delta G_\sigma^{stat+vib} \equiv G_\sigma^{stat+vib} - G_{HS}^{stat+vib}$. Again, when the lattice vibrational contribution is disregarded, we have $\Delta G_\sigma^{stat+vib} = \Delta H_\sigma \equiv H_\sigma - H_{HS}$.

The vibrational free energy: the Vibrational Virtual Crystal Model (VVCM)

The quasiharmonic approximation (QHA) (Wallace 1972) is a good approximation for most mantle minerals at relevant conditions. Its performance is reviewed in this volume (Wentzcovitch et al. 2010). Within the QHA, the free energy is given by:

$$F(V,T) = \left[U(V) + \sum_{\mathbf{q},j} \frac{\hbar\omega_{\mathbf{q},j}(V)}{2}\right] + k_B T \sum_{\mathbf{q},j} \log\left[1 - \exp\left(-\frac{\hbar\omega_{\mathbf{q},j}(V)}{k_B T}\right)\right] \tag{11}$$

where $U(V)$ and $\omega_{\mathbf{q},j}(V)$ are the volume-dependent static internal energy and the phonon spectrum. Once $F(V,T)$ is known, other thermodynamic quantities, such as pressure and Gibbs free energy, can be derived. For the systems that can be treated using standard DFT, such as MgO, the interatomic force constants $D_{\mu\nu}^{ij}$, which is defined as

$$D_{\mu\nu}^{ij} = \frac{\partial^2 E}{\partial R_i^\mu \partial R_j^\nu} \tag{12}$$

can be calculated by first principles using density-functional perturbation theory (DFPT) (Baroni et al. 2001). In Equation (12), R_i^μ and R_j^ν denote the μ^{th} and ν^{th} Cartesian components of the positions of atom *i* and *j*, respectively. With the computed interatomic force constants, the phonon dispersion relation can be determined by the formula

$$\det\left|\frac{\tilde{D}_{\mu\nu}^{ij}(\mathbf{q})}{\sqrt{M_i M_j}} - \omega_{\mathbf{q}}^2\right| = 0 \tag{13}$$

where the dynamical matrix $\tilde{D}_{\mu\nu}^{ij}(\mathbf{q})$ is defined as

$$\tilde{D}_{\mu\nu}^{ij}(\mathbf{q}) \equiv \sum_{i,j} \exp\left[-i\mathbf{q}\cdot(\mathbf{R_i} - \mathbf{R_j})\right] D_{\mu\nu}^{ij} \tag{14}$$

Unfortunately, DFPT is not currently implemented in combination with DFT+*U*. Moreover, calculations of vibrational density of states (VDoS) of solid solutions are not straightforward. Therefore, another reasonably accurate approach to calculate the vibrational VDoS of these systems is needed. Wu et al. (2009) developed a vibrational virtual-crystal model (VVCM) to calculate the phonon spectrum and thermodynamic properties of ferropericlase at temperatures up to 4000 K and pressures up to 150 GPa.

In the VVCM, the cations forming the solid solution, i.e., magnesium and iron, are replaced by an "average" cation that reproduces the same vibrational properties of the solid solution,

$$M_{VC}^{cation} = (1 - X_{Fe})M_{Mg} + X_{Fe}M_{Fe} \tag{15}$$

where M_{Mg} and M_{Fe} are the mass of magnesium and iron, respectively. Therefore, the VVCM has only two atoms per unit cell of the rocksalt structure. The next question is how to determine the interatomic force constants between the atoms in the virtual crystal. Within DFT+U, the elastic constants of the actual solid solution, $C_{\sigma\tau\alpha\beta}$, can be calculated using stress-strain relation. The acoustic wave velocities, v, along several directions can then be determined using Crystoffel's equation,

$$\det\left|C_{\sigma\tau\alpha\beta}n_\tau n_\beta - \rho v^2 \delta_{\sigma\alpha}\right| = 0 \tag{16}$$

where $\mathbf{n}$, ρ, and δ are the wave propagation direction, mass density, and Kroenecker delta, respectively. Starting from the elastic constants of MgO, its largest nearest neighbor interatomic force constants of the virtual crystal are varied. The dynamical matrix, phonon dispersions, and the acoustic wave velocities

$$v[\mathbf{n}] = \frac{d\omega_{\mathbf{q}}}{d\mathbf{q}}[\mathbf{n}]\Big|_{\mathbf{q}=0} \tag{17}$$

vary accordingly. The appropriate interatomic force constants of the virtual crystal are those that give the wave velocities (Eqn. 17) matching the wave velocities of the actual solid solution (Eqn. 16). With this set of appropriately chosen interatomic force constants, the phonon spectrum and the vibrational density of states can be determined accordingly. The thermodynamic properties of ferropericlase calculated using this method will be shown in the next section.

Computational details

In ferropericlase (Tsuchiya et al. 2006; Wentzcovitch et al. 2009; Wu et al. 2009), the computations were performed using the LDA (Ceperley and Alder 1980; Perdew and Zunger 1981). The oxygen pseudopotential was generated by the method of Troullier-Martins (Troullier and Martins 1991) with core radii $r(2s) = r(2p) = 1.45$ a.u in the configuration $2s^2 2p^4$ with p locality. The magnesium pseudopotential was generated by the method of von Barth-Car. Five configurations, $3s^2 3p^0$, $3s^1 3p^1$, $3s^1 3p^{0.5} 3d^{0.5}$, $3s^1 3p^{0.5}$, and $3s^1 3d^1$ with decreasing weights 1.5, 0.6, 0.3, 0.3, and 0.2, respectively, were used. Core radii were $r(3s) = r(3p) = r(3d) = 2.5$ a.u. with d locality. The ultrasoft pseudopotential for iron was generated using the modified Rappe-Rabe-Kaxieas-Joannopoulos (RRKJ) scheme (Rappe et al. 1990). Core radii were $r(4s) = (2.0, 2.2)$, $r(4p) = (2.2, 2.3)$, and $r(3d) = (1.6, 2.2)$ a.u. in the configuration $3d^7 4s^1$, where the first and second numbers in each parenthesis represent the norm-conserving core radius and ultrasoft radius, respectively. All-electron potential pseudized at $r_c < 1.7$ a.u. was taken as a local potential. The plane wave energy cutoff was 70 Ry. Brillouin zone sampling for electronic states was carried out on 8 k-points for the cubic supercell containing 64 atoms. Equivalent k-point mesh were used in 128 and 216 atom calculations for ferropericlase with $X_{\mathrm{Fe}} = 0.0625$ and 0.03125.

For $(Mg,Fe)SiO_3$ perovskite (Umemoto et al. 2008, 2009; Hsu et al. 2009b), the computations used both LDA (Ceperley and Alder 1980; Perdew and Zunger 1981) and (PBE) GGA (Perdew et al. 1996). The pseudopotentials for Fe, Si, and O were generated by Vanderbilt's method (Vanderbilt 1990). The valence electronic configurations used were $3s^2 3p^6 3d^{6.5} 4s^1 4p^0$, $3s^2 3p^1$, and $2s^2 2p^4$ for Fe, Si, and O, respectively. The pseudopotential for Mg is the same as the one used for ferropericlase. The plane wave cutoff energy was 40 Ry. In each supercell being used, the k-point mesh is fine enough to achieve convergence within 1 mRy/Fe in the total energy. Variable-cell-shape molecular dynamics (Wentzcovitch et al.

1993) implemented in QUANTUM-ESPRESSO package (Giannozzi et al. 2009) is used for structural optimizations. In Hsu et al. (2009b), the electric field gradient (EFG) tensors are calculated using the augmented plane wave + local orbitals (APW+lo) method (Madsen et al. 2001) implemented in the WIEN2k code (Blaha et al. 2001), and they are converted to the QS values using Q = 0.16 barn (Petrilli et al. 1998).

SPIN-STATE CROSSOVER IN FERROPERICLASE

The pressure-induced spin-state crossover (HS-to-LS) of iron in ferropericlase was already observed in many types of experiments, including experiments that probe the electronic states of ferropericlase, such as X-ray emission spectroscopy (XES) (Badro et al. 2003; Lin et al. 2005, 2006a, 2007a,c; Vanko and de Groot 2007) and X-ray absorption near-edge spectroscopy (XANES) (Kantor et al. 2009; Narygina et al. 2009), and experiments that probe the asymmetry of electron charge distribution around the iron nucleus, such as Mössbauer spectroscopy (Gavriliuk et al. 2006; Kantor et al. 2006, 2007, 2009; Lin et al. 2006a; Speziale et al. 2005). Several physical quantities of ferropericlase are affected by the spin-state crossover, including the enhancement of density (reduction of volume) observed in X-ray diffraction (Fei et al. 2007; Lin et al. 2005; Speziale et al. 2005, 2007), variation of sound velocity observed in nuclear resonant inelastic X-ray scattering (Lin et al. 2006b), enhanced absorption in the mid- and near-infrared range (Goncharov et al. 2006; Keppler et al. 2007), change of elastic properties observed using impulsive stimulated scattering (Crowhurst et al. 2008), and decrease of electrical conductivity (Lin et al. 2007b). Using Mössbauer spectroscopy, the effect of temperature and pressure on the quadrupole splitting of the iron nucleus was studied as well (Kantor et al. 2009; Lin et al. 2009). The transition pressures observed in these experiments are not exactly the same, depending on both the iron concentration and the experimental techniques. The room-temperature XES spectra of samples with different iron concentration show that the transition pressure increases with iron concentration (Lin et al. 2005, 2006a, 2007a; Vanko and de Groot 2007). For the various experiments (XES, Mossbauer, and optical absorption) with iron concentration close to that in the lower mantle (17%), the transition pressure at room temperature mainly ranges from 50 to 70 GPa (Goncharov et al. 2006; Kantor et al. 2006; Lin et al. 2005, 2006a; Speziale et al. 2005; Vanko and de Groot 2007). A lower transition pressure of 30 GPa, however, is also observed in the X-ray diffraction experiment by Fei et al. (2007).

The dependence of the (static) transition pressure on iron concentration was studied theoretically using GGA+U (Persson et al. 2006) and LDA+U methods (Tsuchiya et al. 2006). In Persson et al. (2006), high iron concentrations ($X_{Fe} > 0.25$) were considered. The Hubbard U was chosen to be 3.0 and 5.0 eV. Irrespective of U, the transition pressure increased with X_{Fe}, while the transition pressures for U = 3.0 eV were smaller than those given by U = 5.0 eV, irrespective of X_{Fe}. In Tsuchiya et al. (2006), the Hubbard U was determined by first principles (Cococcioni and de Gironcoli 2005). The transition pressure was not sensitive to X_{Fe} for $X_{Fe} < 0.1875$ for uniformly distributed iron configurations. In these configurations irons interacted weakly, which suggested the use of an ideal solid solution model would be a good approximation to investigate the thermodynamics of the spin crossover (Tsuchiya et al. 2006). The sensitivity of the transition pressure to X_{Fe} for $X_{Fe} > 0.25$ might be cause by iron-iron interaction (Kantor et al. 2009) but might also be understood, at least in part, as the effect of chemical pressure caused by magnesium. The latter is smaller than ferrous iron in the HS state. The lattice parameter of the (Mg,Fe)O solid solution increases with X_{Fe}. Therefore, solid solutions with large X_{Fe} need to be compressed further to induce the HS-to-LS crossover triggered by a critical Fe-O distance. The effect of iron-iron interaction in ferropericlase still deserves further investigation to clarify this point. A comparison between the DFT+U calculations (Persson et al. 2006; Tsuchiya et al. 2006) and experiments using XES (Lin et al. 2005, 2006a) and Mössbauer spectroscopy (Badro et al. 1999; Pasternak et al. 1997;

Speziale et al. 2005) is shown in Figure 1 (Persson et al. 2006). Thermodynamic properties of ferropericlase at various temperatures and pressures were computed by first principles in Wu et al. (2009) and Wentzcovitch et al. (2009), using the Hubbard U obtained by Tsuchiya et al. (2006). These results are summarized in the next sub-sections.

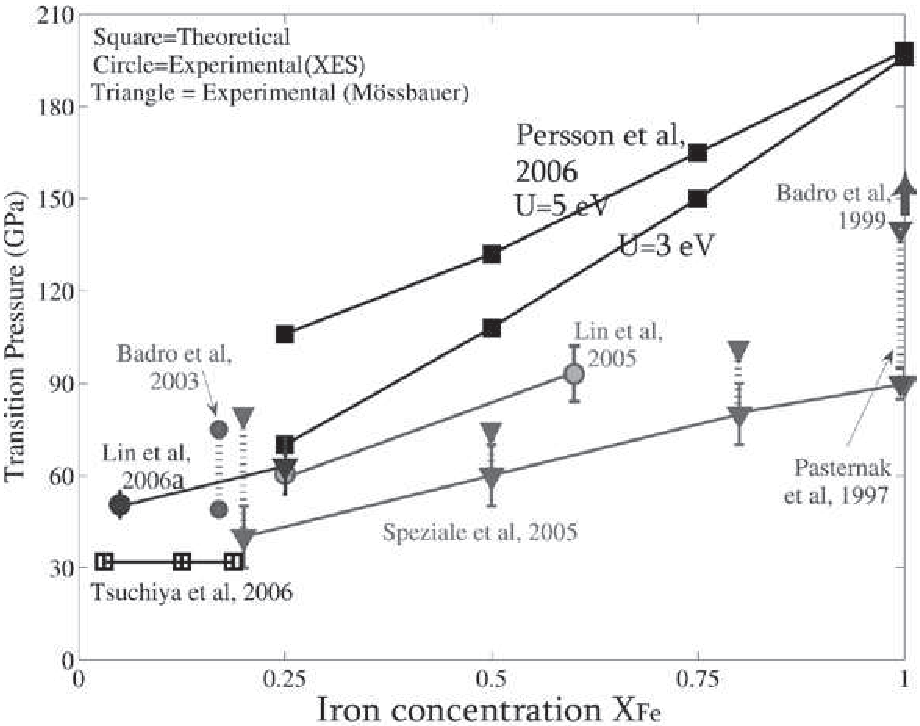

Figure 1. Dependence of the HS-to-LS transition pressure of ferropericlase on the iron concentration. The computational results by Persson et al. (2006) and Tsuchiya et al. (2006) are both shown along with various experiments. The transition pressured from Speziale et al. 2005 were measured at 6-300 K, while others were all room temperature measurements. [Used by permission of AGU, from Persson et al. (2006)].

Static LDA+U calculation

In Tsuchiya et al. (2006), the LDA+U method was used to calculate the atomic and electronic structure of ferropericlase with various iron concentration and different unit-cell volumes. The Hubbard U was determined from the linear response of the occupation matrix to a potential shift at the iron site. As shown in Figure 2, the computed Hubbard U is spin and volume dependent. The effect of iron concentration, X_{Fe}, is less significant and the Hubbard Us can be fitted to a single function of unit-cell volume, V, to first order. The distinguishing factor is the spin state.

When the on-site Coulomb interaction (Hubbard U) is included, desirable atomic structure and orbital occupancies are obtained, as shown in Figure 3. In the HS case, the five majority-spin d-electrons occupy the five d-orbitals to give spherical majority charge distribution, while the minority-spin electron occupies the d_{xy} orbital and induces greater Fe-O distance on the xy plane. This Jahn-Teller distortion does not happen in LDA. In LDA, all Fe-O distances are the same, and all three t_{2g} orbitals are degenerate and equally occupied by the minority-spin electron. Due to the partially-filled t_{2g} band, the HS ferropericlase is half-metallic in LDA. Such difference in orbital occupancy between LDA and LDA+U can be understood on the basis of the DFT+U energy functional of Equation (1). When U is included, each d-orbital tends to be completely filled or empty to minimize E. Thus, the minority-spin electron in HS iron tends to completely occupy one of the t_{2g} orbitals and induce J-T distortion, instead of partially

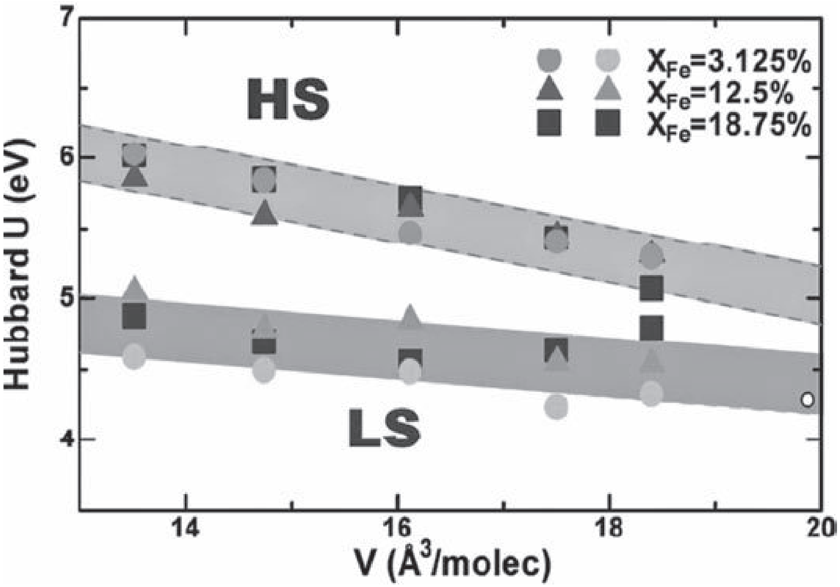

Figure 2. Computed Hubbard U of iron in ferropericlase as a function of unit-cell volume. The Hubbard U is not very sensitive to the iron concentration. Open circle is the U of HS iron in FeO. [Used by permission of APS, from Tsuchiya et al. (2006)].

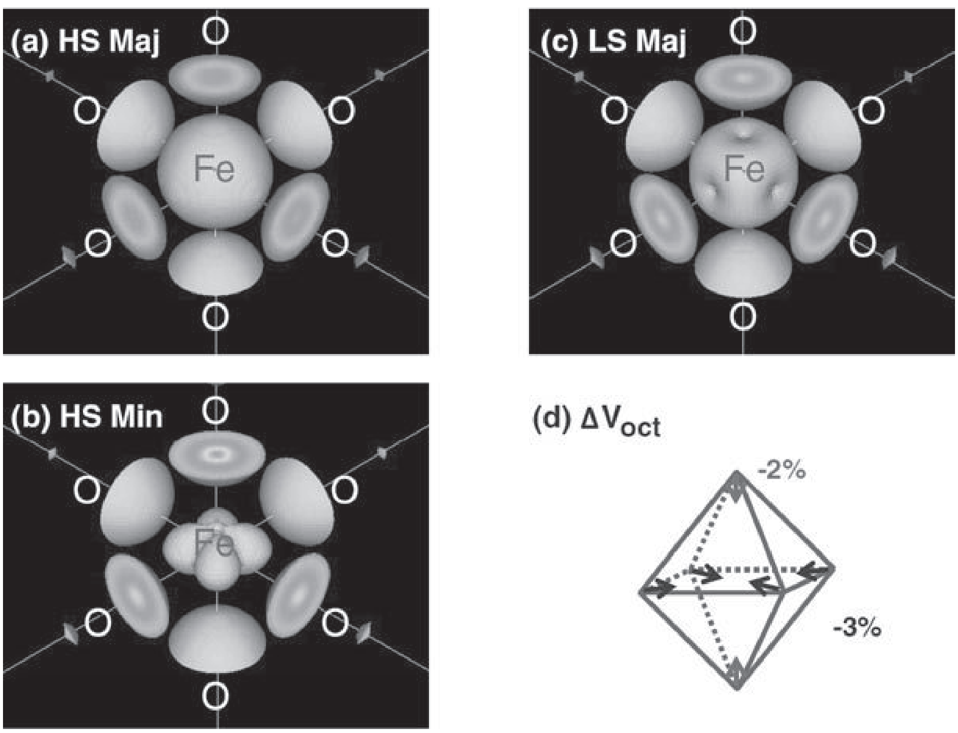

Figure 3. Charge density around iron in ferropericlase with 12.5% of iron. (a) HS majority; (b) HS minority; (c) LS majority; and (d) depiction of the polyhedral volume collapse across the spin transition. The isosurface value is 0.3 e/Å^3. [Used by permission of APS, from Tsuchiya et al. (2006)].

occupying three degenerate t_{2g} orbitals as in LDA. The J-T distortion splits the t_{2g} derived level into a singlet, the d_{xy} "band", and a doublet, the d_{yz} and d_{xz} "bands". With a completely filled d_{xy} band, HS ferropericlase is an insulator in LDA+U. The charge distribution shown in Figures 3(a-c) also implies a sudden decrease of volume when the HS-to-LS crossover occurs. The octahedral volume reduction is ~8% (see Fig. 3d).

Spin-state transition can be clearly observed in static calculation, as shown in Figure 4. By plotting the relative enthalpies of pure HS with respect to pure LS ferropericlase for different iron concentrations, X_{Fe}, it is shown in Figure 4(a) that the HS-to-LS static "transition" pressure P_t is not sensitive to the iron concentration X_{Fe}. Within $0.03125 < X_{Fe} < 0.1875$, P_t is about 32 GPa. Figure 4(b) displays the relative enthalpy of mixed-spin (MS) states for X_{Fe} = 0.1875 with various LS fractions, n. Figure 4(c) shows the zero temperature static compression curves of these MS states and the experimental data in Lin et al. (2005). The experimental data shows anomalous volume reduction accompanying with spin-state crossover. In this set of experimental data, the transition occurs at 54-67 GPa. In the other experiment, however, the transition pressure is as low as 35 GPa (Fei et al. 2007). These experiments were performed at room temperature while these results were obtained in static calculations. As shall be seen below, inclusion of vibrational effects can greatly improve agreement between calculations and experiments.

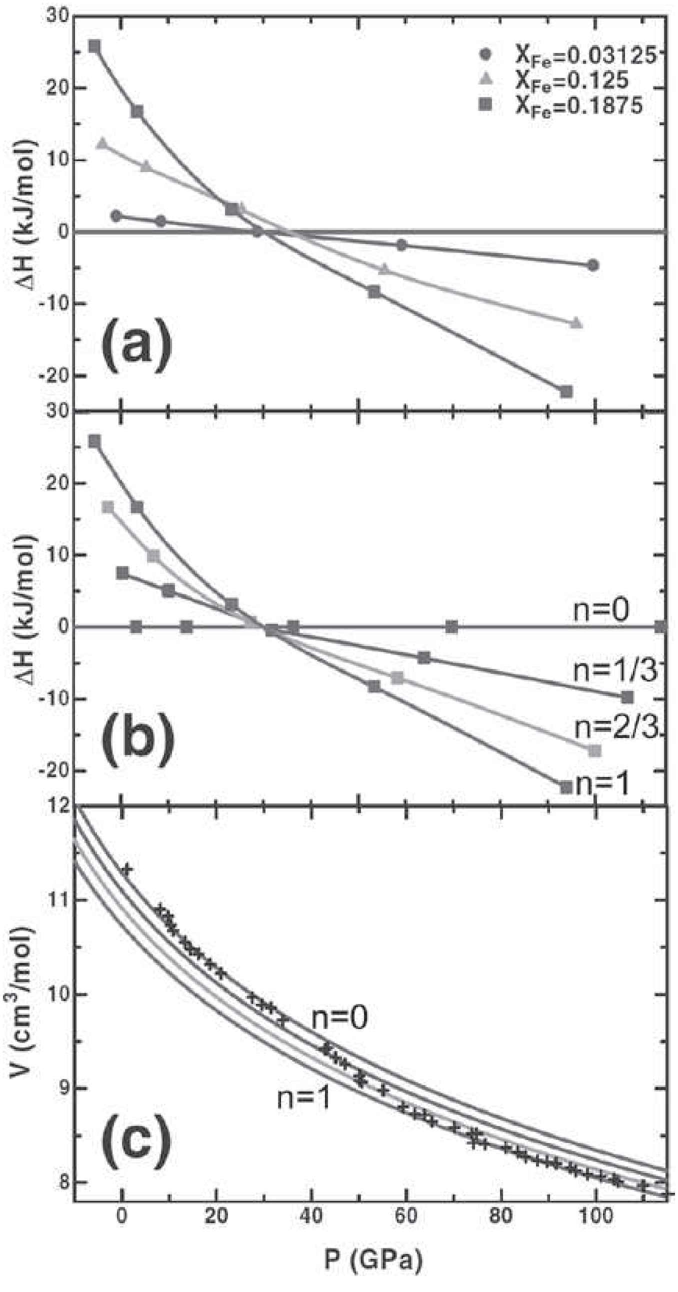

Figure 4. (a) Static enthalpy difference between LS and HS phases at three different iron concentrations. (b) Enthalpy difference in ferropericlase with iron concentration of 18.75% between states with various fractions of LS iron, n. The reference line corresponds to the enthalpy of all irons in HS state (n = 0). (c) Pressure-volume curves of ferropericlase with 18.75% of iron at different fraction of LS iron. The plus signs are experimental results at 300 K with 17% of iron by Lin et al. (2005). [Used by permission of APS, from Tsuchiya et al. (2006)].

VVCM for ferropericlase

A vibrational virtual crystal model was engineered to give the average vibrational properties of and acoustic velocities of the ferropericlase solid solution of in pure HS and LS states. Only the VDoSs of the pure spin states are necessary to proceed with the thermodynamics calculation outlined in the previous section. Both ferropericlase and MgO are cubic systems and have only three elastic constants, C_{11}, C_{12}, and C_{44} (in Voigt notation). The longitudinal (v_L) and transverse (v_T) wave velocities along the [100] direction are

$$\begin{aligned} v_L &= \omega_L / q = \sqrt{C_{11} / \rho} \\ v_T &= \omega_T / q = \sqrt{C_{44} / \rho} \end{aligned} \tag{18}$$

and along the [100] direction are

$$\begin{aligned} v_L &= \sqrt{\left(C_{11} + C_{12} + C_{44}\right) / 2\rho} \\ v_{T1} &= \sqrt{C_{44} / \rho} \\ v_{T2} &= \sqrt{\left(C_{11} - C_{12}\right) / 2\rho} \end{aligned} \tag{19}$$

For ferropericlase, all three static elastic constants can be calculated with LDA+U. The next step is to choose the force constant in the virtual crystal to reproduce these wave velocities. The most relevant force constants, $D^{ij}_{\mu\nu}$, in the virtual crystal are shown in Figure 5. They are: (a) the Mg-O nearest-neighbor longitudinal constant, D^{12}_{xx}, (b) the Mg-O nearest-neighbor transverse constant, D^{23}_{xx}, and (c) the Mg-Mg nearest neighbor magnesium interaction constant, D^{24}_{xy}. Their values are listed in Table 1. All other force constants have minor effects in the acoustic dispersion. The three force constants, D^{13}_{xx}, D^{16}_{xx}, and D^{13}_{zz}, are between the oxygen

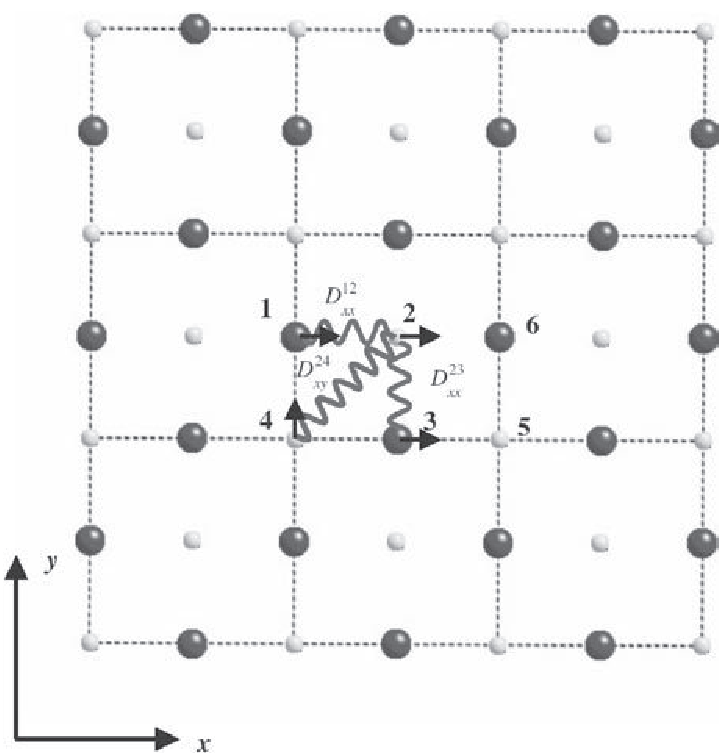

Figure 5. Schematic representation of the three largest force constants of MgO in *xy* plane. See text for the definition of these constants. The oxygen and magnesium atoms are represented by the large and small spheres, receptively. [Used by permission of APS, from Wu et al. (2009)].

Table 1. The eight largest force constants of MgO and their modified values for ferropericlase in HS and LS states. These values were obtained for the lattice constant of 4.07 Å (Wu et al. 2009).

	D_{xx}^{12}	D_{xy}^{24}	D_{xx}^{23}	D_{xx}^{13}	D_{xx}^{45}	D_{xx}^{24}	D_{xx}^{16}	D_{zz}^{13}
MgO	–0.1517	–0.0153	0.0117	–0.0078	–0.0054	–0.0047	0.0046	–0.0034
HS	–0.1570	–0.0167	0.0173	–0.0078	–0.0054	–0.0047	0.0046	–0.0034
LS	–0.1571	–0.0118	0.0162	–0.0078	–0.0054	–0.0047	0.0046	–0.0034

atoms, and the replacement of Mg by Fe in the virtual crystal affects these forces very little. D_{xx}^{45} and D_{xx}^{24} are between Mg and O, but they are much smaller than the three major force constants, D_{xx}^{12}, D_{xy}^{24}, and D_{xx}^{23}. Other force constants that are not presented are even smaller than the ones shown in Table 1. Therefore, only the three major force constants are modified to describe ferropericlase in pure spin states.

The elastic constants and the bulk modulus obtained by first-principles in LDA+*U* and the ones obtained from the reproduced phonon velocities in the virtual crystals are shown in Figure 6. They agree with each other very well. Therefore the VVCM's acoustic phonon dispersions are precisely the same as those of HS and LS ferropericlase. The VDoS obtained using VVCM for the case with lattice constant 4.21 Å is shown in Figure 7. The agreement between the result obtained using VVCM method and LDA+*U* (Fig. 6) ensures that the thermodynamic properties are calculated using the correct VDoS at low frequencies and with a reasonably

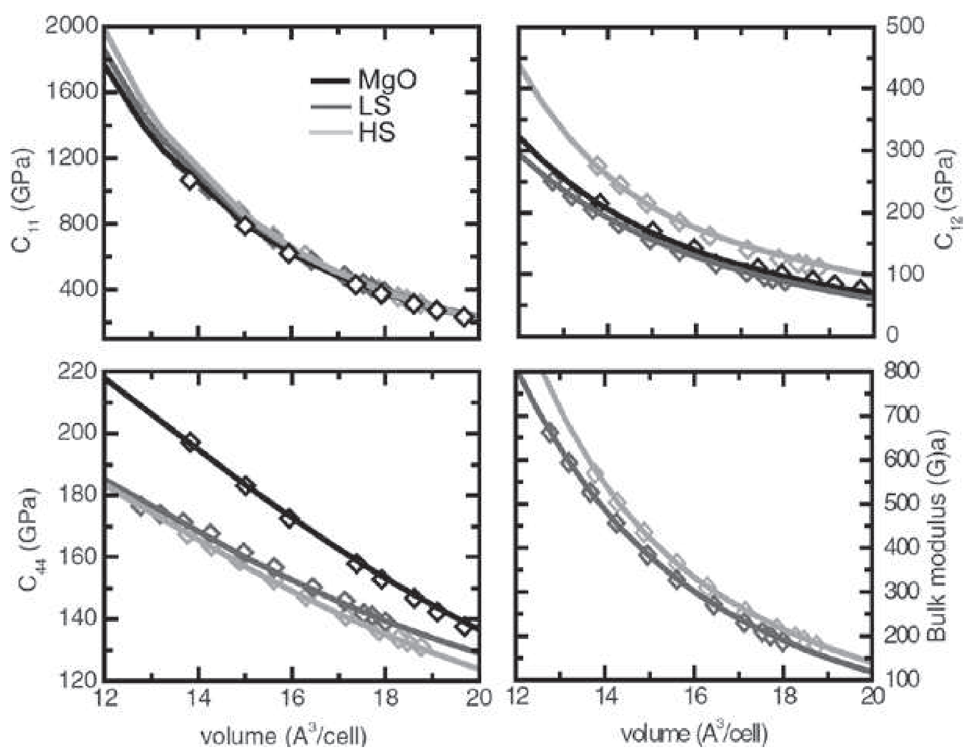

Figure 6. Elastic constants obtained by first principles from the stress-strain relation (symbols) and from phonon velocities (lines).The acoustic phonon velocities of MgO are computed directly using DFPT. The phonon velocities of ferropericlase in HS and LS were obtained by modifying the force constants of MgO. [Used by permission of APS, from Wu et al. (2009)].

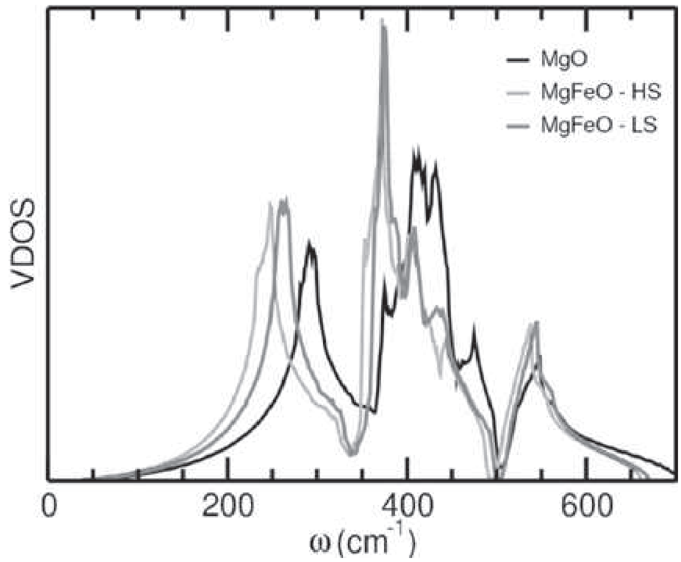

Figure 7. Vibrational density of states of MgO and ferropericlase in HS and LS states. These VDoS were computed with lattice parameter a = 4.21 Å. [Used by permission of APS, from Wu et al. (2009)].

good, i.e., representative, VDoS at high frequencies. The VVCM in conjunction with the QHA should provide more suitable vibrational and thermodynamic properties than a Mie-Debye-Gruneisen model.

Before presenting the thermodynamics properties of ferropericlase, the pressure and temperature range of the validity of QHA should be addressed. It is determined by *a posteriori* inspection of the thermal expansion coefficient, $\alpha \equiv (1/V)(\partial V/\partial T)|_P$, of ferropericlase in MS state. This method is discussed in the paper on quasiharmonic thermodynamics properties of minerals in this book. For ferropericlase in MS state, the volume as a function of the LS iron fraction $n \equiv n_{LS}(P,T)$ is determined by the derivative of Gibbs free energy with respect to pressure at a fixed temperature,

$$V(n) = \left.\frac{\partial G(n)}{\partial P}\right|_T = \left.\frac{\partial G(n)}{\partial P}\right|_{T,n} + \left.\frac{\partial G(n)}{\partial n}\right|_{T,P} \left.\frac{\partial n}{\partial P}\right|_T \tag{20}$$

At equilibrium, the term $\partial G/\partial n|_{T,P}$ vanishes, so the volume is

$$V(n) = nV_{LS} + (1-n)V_{HS} \tag{21}$$

where $V_{LS/HS} \equiv \partial G_{LS/HS}/\partial P|_T$ are the volumes of the pure LS/HS states, and the HS fraction $n_{HS} = 1 - n$. The thermal expansion coefficient of the MS ferropericlase is then

$$\alpha V(n) = nV_{LS}\alpha_{LS} + (1-n)V_{HS}\alpha_{HS} + (V_{LS} - V_{HS})\left.\frac{\partial n}{\partial T}\right|_P \tag{22}$$

The upper temperature limit of the validity of QHA at a certain pressure can be indicated by the inflection point of α with respect to temperature, namely, $\partial^2\alpha/\partial T^2|_P = 0$ (Carrier et al. 2008; Wentzcovitch et al. 2004). Beyond this inflection point, the thermal expansivity deviates from the usually linear behavior of experimental measurements. The temperature limits for ferropericlase in the pure LS and HS states are first established. The thermal expansion coefficient of MS state is determined from Equation (22). The maximum temperature limit for the predictions in the MS state is chosen as the minimum of those established for the HS and LS states.

Thermodynamic properties of ferropericlase

All methods discussed in previous sections provide a fine description of ferropericlase in the MS state at finite temperatures and pressures, as can be confirmed by the agreement between the computed (Wu et al. 2009) and experimental (Lin et al. 2005; Fei et al. 2007) isothermal compression curves shown in Figure 8. At 300 K, the calculated isotherm displays anomaly in $V(P,T,n)$ consistent with the experimental results. The theoretical equilibrium volume at 300 K, 11.46 cm^3/mol, is slightly larger than the experimental one, 11.35 cm^3/mol. This volume difference is consistent with the difference of iron concentration in the experiments (0.17) and calculation (0.1875). The predicted volume reduction resulting from the spin-state transition is 4.2% for $X_{Fe} = 0.1875$, compared to about 3-4% in experiments.

The fraction of LS irons as a function of pressure and temperature, $n(P,T)$, in ferropericlase with $X_{Fe} = 0.1875$ is shown in Figure 9. At 0 K, the transition occurs at ~36 GPa, and it is very sharp. As the temperature increases, the pressure at the center of the crossover range increases, and the crossover broadens. The black (white) line corresponds to $n(P,T) = 0.5$ in calculations including (without) the vibrational contribution to the free energy. Even at 0 K the transition pressure increases by 2.5 GPa because of zero-point motion energy. At 300 K, the center of the crossover occurs at 39.5 GPa, which agrees with data by Fei et al. (2007), but differs from many other experiments showing a transition pressure around 50-55 GPa (Goncharov et al. 2006;

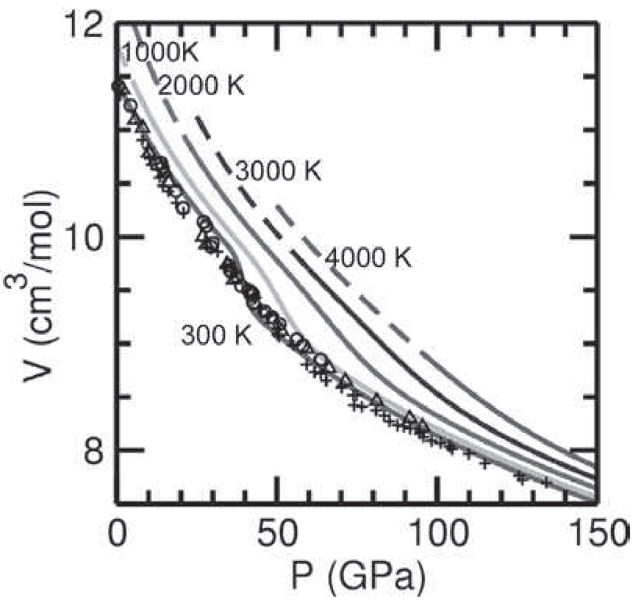

Figure 8. Compression curves of ferropericlase with iron concentration of 18.75% along several isotherms. Solid (dashed) lines correspond to the results within (outside) the (P,T) regime of the validity of QHA. Plus symbols are experimental results adopted from Lin et al. (2005), with iron concentration of 17%. The circle and triangle symbols are the results presented in Fei et al. (2007), with iron concentration of 20%. [Used by permission of APS, from Wu et al. (2009)].

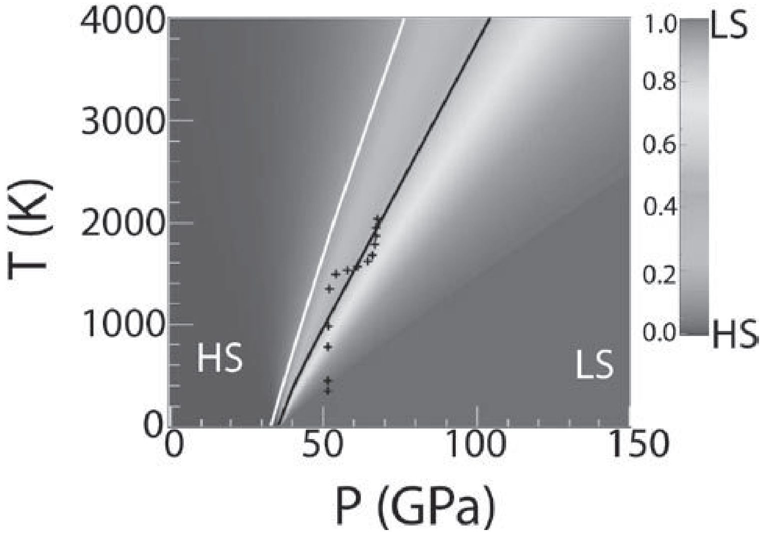

Figure 9. The LS iron fraction as a function of pressure and temperature, $n(P,T)$, in ferropericlase with iron concentration of 18.75%. The black (white) line corresponds to the middle point of the crossover, namely, $n(P,T) = 0.5$, with (without) the inclusion the vibrational contribution in the free energy. In other words, along the black (white) line, the relation $\Delta G_{LS} = 0$ ($\Delta H_{LS} = 0$) holds. The plus symbols are the experimental data corresponding to $n(P,T) = 0.5$ presented in Lin et al. (2007c). [Used by permission of APS, from Wu et al. (2009)].

Kantor et al. 2006; Lin et al. 2005, 2006a; Speziale et al. 2005; Vanko and de Groot 2007). The computed transition pressure may still improve after a more complete treatment of the solid solution and after a more accurate Hubbard U is calculated self-consistently, as mentioned earlier.

Figure 10 shows the thermal expansion coefficient α, constant-pressure heat capacity C_P, and thermal Grüneisen parameter γ, of ferropericlase along several isobars. At very low or very high pressure, α looks "normal" since in these two extremes ferropericlase is in essentially pure HS and LS states, respectively. The normal α of HS ferropericlase is the same as that of MgO (Touloukian et al. 1977). In the temperature range when QHA is valid ($T < 1500$ K), the computed α agrees with that of ferropericlase up to $X_{Fe} = 0.36$ (van Westrenen et al. 2005). Comparing Figures 9 and 10, we can see that anomalies occur in the crossover region, namely, in the MS state. Similar anomalous behavior can be observed in heat capacity and thermal Grüneisen parameter in the same pressure and temperature range, only that the anomaly in C_P is not as dramatic as in α and γ.

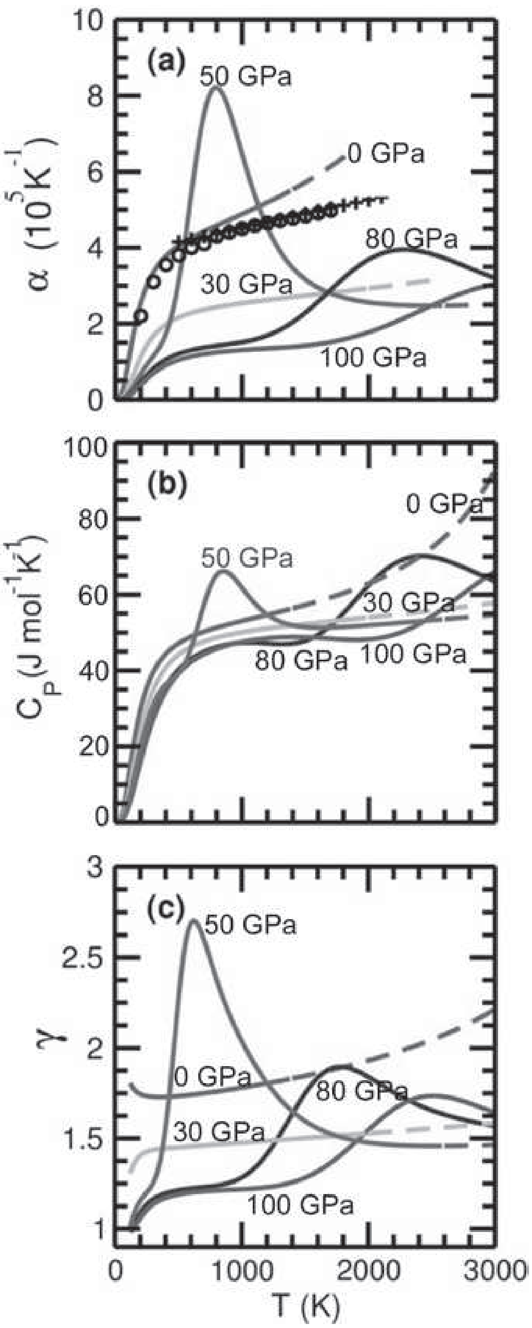

Figure 10. (a) Thermal expansion coefficient; (b) constant-pressure heat capacity; and (c) thermal Grüneisen parameter of ferropericlase with iron concentration of 18.75% along several isobars. Solid (dashed) lines correspond to the results within (outside) the (P, T) regime of validity of the QHA. Circles and crosses are the experimental values at 0 GPa for ferropericlase with iron concentration of 0% (Touloukian et al. 1977) and 36% (van Westrenen et al. 2005), respectively. [Used by permission of APS, from Wu et al. (2009)].

The fraction of LS irons along several isotherms is shown in Figure 11. Along with Equations (20)-(22), it provides useful information to understand the anomalous behavior in several physical quantities shown in Figure 12, including the softening of the adiabatic bulk modulus K_s, the sudden decrease in bulk wave velocity, $v_φ$, and the enhancement of density ρ. The transition is sharper at lower temperature (Fig. 11), and greater anomalies can be observed (Fig. 12) at those temperatures. Below 35 GPa, the calculated ρ at 300 K agrees very well with experiments using samples with $X_{Fe} = 0.17$ (Lin et al. 2005). The remaining difference is consistent with the difference in iron concentrations. The reduction of K_s and $v_φ$ is consistent with experimental data on samples containing $X_{Fe} = 0.06$ (Crowhurst et al. 2008). The larger anomalies in the calculation are consistent experimental data on samples with X_{Fe} three times smaller.

The effect of spin-state crossover in ferropericlase along a typical geotherm (Boehler 2000) is shown in Figure 13(a-b). The anomalies in K_s (25 ± 6%) and $v_φ$ (15 ± 7%) predicted

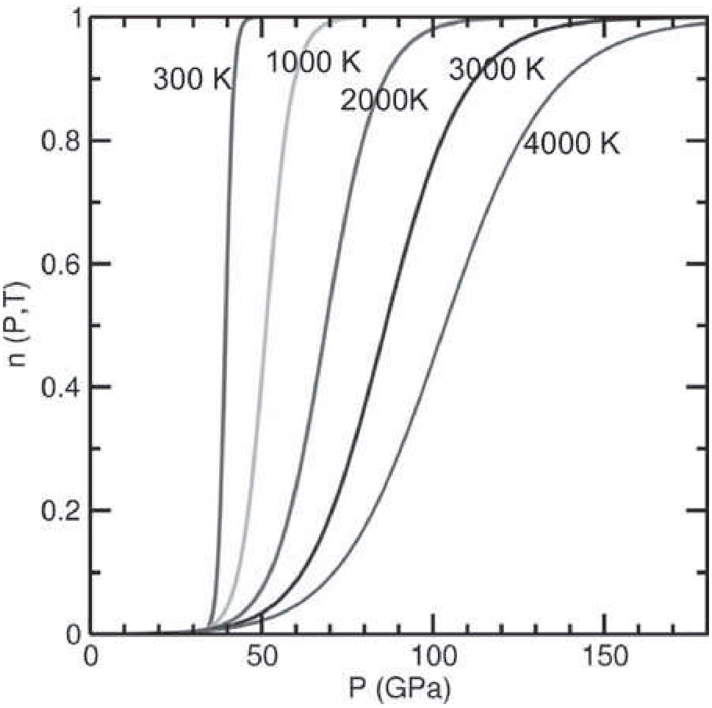

Figure 11. The LS iron fraction, $n(P,T)$, of ferropericlase with iron concentration of 18.75% along several isotherms. At lower temperature, the derivative $\partial n/\partial P|_T$ has greater values. This implies greater anomalous behavior at lower temperatures. [Used by permission of APS, from Wu et al. (2009)].

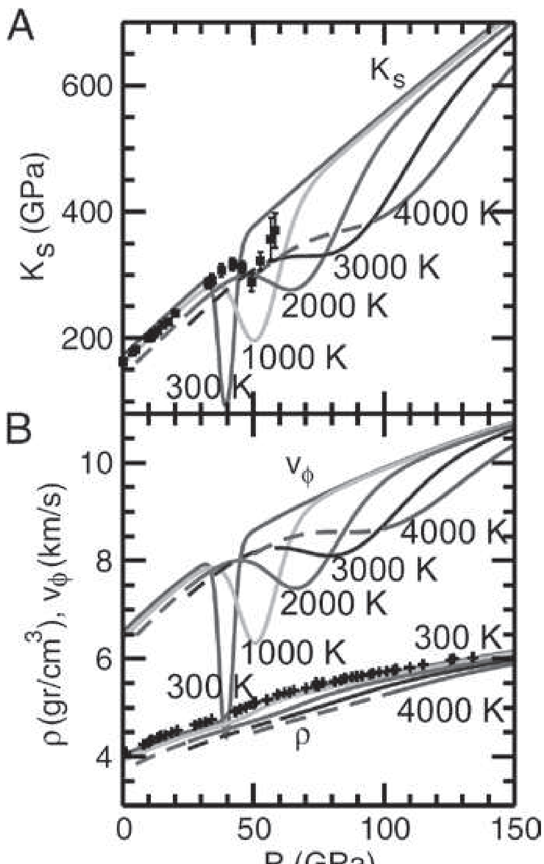

Figure 12. Pressure dependence of the calculated adiabatic bulk modulus K_S (A), bulk wave velocity v_φ, and density ρ (B) of ferropericlase with 18.75% of iron along several isotherms. Solid (dashed) lines correspond to the results within (outside) the (P,T) regime of validity of the QHA. Also presented in (A) are the experimental data of ferropericlase with 6% of iron (Crowhurst et al. 2008). The calculated anomaly is about three times greater than the experiment, agree with the difference of iron concentration. Crosses shown in (B) are the data of ferropericlase with 17% of iron at room temperature (Lin et al. 2005). [Used by permission of National Academy of Sciences, from Wentzcovitch et al. (2009)].

by a purely elastic model start at ≈ 40 GPa (≈ 1000 km depth) and are most pronounced at ≈ 70 ± 20 GPa (≈ 1600 ± 400 km depth), but the crossover continues down to the core-mantle boundary (CMB) pressure with a possible reentrance into the HS state because of the thermal boundary layer above the CMB (Boehler 2000). However, one should have in

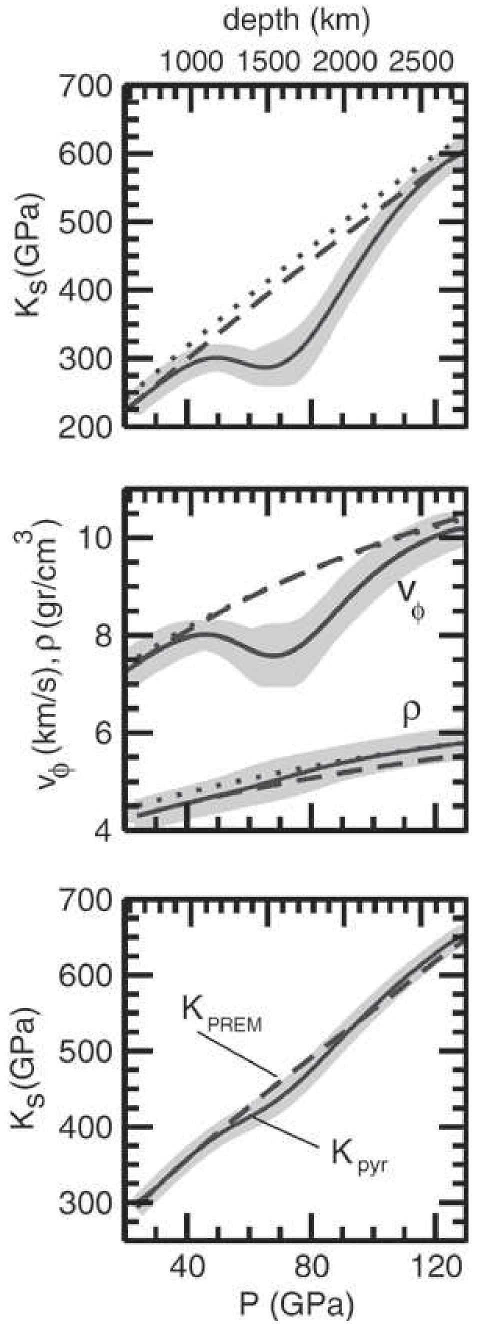

Figure 13. Calculated properties of ferropericlase with 18.75% of iron along a lower mantle geotherm (Boehler 2000). (A) adiabatic bulk modulus K_S; (B) bulk wave velocity v_φ, and density ρ; and (C) bulk modulus of an aggregate with pyrolite composition (McDonough and Sun 1995), K_{pyr}, and PREM's bulk modulus, K_{PREM} (Dziewonski and Anderson 1981). In (A) and (B), solid, dashed, and dotted lines correspond to the properties computed in the MS, HS, and LS states, respectively. Shaded regions represent the uncertainties caused mainly by the uncertainty in the computed enthalpies of HS and LS states and transition pressure at 0 K. [Used by permission of National Academy of Sciences, from Wentzcovitch et al. (2009)].

mind that the bulk modulus softens. In contrast, density increases smoothly throughout the entire pressure range of the lower mantle. The shaded areas correspond to uncertainties caused by uncertainties in the calculated static transition pressure and the narrower crossover pressure range (Wentzcovitch et al. 2009).

The net effect of the spin crossover in ferropericlase on the bulk modulus of a uniform aggregate with pyrolite composition (McDonough and Sun 1995), K_{pyr}, along a typical geotherm (Boehler 2000) is shown in Figure 13(c). This comparison is made to elucidate and highlight an effect that may be quite subtle. The bulk modulus of perovskite calculated by first-principles is adopted (Wentzcovitch et al. 2004) in the calculation of K_{pyr}. Compared with the bulk modulus of the Preliminary Reference Earth Model (PREM) (Dziewonski and Anderson 1981), K_{PREM}, a subtle reduction of about 4% is observed in K_{pyr}, which appears to be smoothed or cut through by K_{PREM}. The uncertainly of K_{pyr} is quite large and permits the signature of the spin-state crossover in ferropericlase to fall within the uncertainty of global seismic constraints. In this sense K_{PREM} does not appear to be inconsistent with the calculated K_{pyr} along the geotherm.

An intriguing possibility of a viscosity anomaly caused by this crossover in the mantle has been raised (Wentzcovitch et al. 2009). In a well mixed mantle, phase separation between ferropericlase and perovskite is expected to occur owing to the contrast in their rheological properties (Barnhoorn et al. 2005; Holtzman et al. 2003; Yamazaki and Karato 2001). In this situation, the softer phase, ferropericlase, is expected to dominate the rheology of the region. The softening of the bulk modulus in ferropericlase is most enhanced at ~1,500 km depth (Fig. 13). Viscosity profiles for the mantle with viscosity minima around 1,500 have been proposed (Forte and Mitrovica 2001; Mitrovica and Forte 2004) and have been difficult to explain. This spin crossover in ferropericlase may offer an interpretation for this proposed viscosity minimum in the mantle, but in-depth studies of this phenomenon are still needed.

SPIN-STATE CROSSOVER IN FERROSILICATE PEROVSKITE

In contrast to ferropericlase, the detailed mechanism of the spin crossover in iron-bearing magnesium silicate perovskite is still controversial. Various experimental techniques have been used to study this phenomenon in iron in perovskite, including XES (Badro et al. 2004; Li et al. 2004), XANES (Narygina et al. 2009), and Mössbauer spectroscopy (Jackson et al. 2005; Lin et al. 2008; McCammon et al. 2008). In contrast to the conclusive HS-to-LS transition in ferropericlase observed in experiments, there is still a lack of consensus regarding the nature of the spin state change in perovskite. In Badro et al. (2004), the XES spectra of $(Mg_{0.9}Fe_{0.1})SiO_3$ suggested a two-step transition. At 70 GPa, iron changes from pure HS to a MS state, and at 120 GPa, all irons fall to the LS state. The sample in this experiment contained ferrous and ferric iron. In Li et al. (2004), both $(Mg_{0.92}Fe_{0.09})SiO_3$ and $(Mg_{0.87}Fe_{0.09})(Si_{0.94}Al_{0.10})O_3$ samples show a broad crossover, and the non-vanishing satellite peak in the XES spectra measured at 100 GPa was attributed to the existence of IS iron. In XANES spectra (Narygina et al. 2009), a crossover in the 30-87 GPa range was observed, but the spin state of iron was not unambiguously determined. The Mössbauer studies by Jackson et al. (2005) suggested that ferrous iron remains in HS state at all pressures, and the spin crossover occurs only in ferric iron. In contrast, the Mössbauer spectra of the $(Mg_{0.88}Fe_{0.12})SiO_3$ sample presented in McCammon et al. (2008) showed the existence of a "new" species of iron with a quadrupole splitting (QS) of 3.5 mm/s. It was suggested that this high-QS iron is in the IS state, the "HS-to-IS transition" occurs at 30 GPa, and the iron remains in the IS state up to 110 GPa. The IS iron at high pressure was also inferred from a Mössbauer study (Lin et al. 2008). These discrepancies result mainly from the more complex nature of perovskite compared with ferropericlase. In ferropericlase, ferrous iron replaces magnesium and occupies clearly the octahedral site. In perovskite, however, iron can be in ferrous or ferric states, without an accurately known partitioning. Ferrous iron is widely believed to occupy the 8-12 coordinated dodecahedral site (A site), while ferric iron can occupy the dodecahedral or the octahedral site (B site). The fraction and occupancy of ferric irons also depend on the presence of aluminum. To say the least, the existence of an intermediate-spin ferrous iron is uncertain. While some experiments were interpreted as providing evidence in support of IS iron, (Lin et al. 2008; McCammon et al. 2008), theoretical calculations clearly indicate the opposite. First-principles calculations show that IS iron is the least energetically favorable state, and the HS-to-IS crossover should not occur in the pressure range of the lower mantle (Bengtson et al. 2009; Hsu et al. 2009b, Umemoto et al. 2009b). Also, the computed QS of IS ferrous iron is much smaller than that observed in experiments (Bengtson et al. 2009; Hsu et al. 2009b), as shall be discussed later.

In an attempt to better understand the spin-state crossover in perovskite and interpret the experimental results, several calculations were performed, but they are not always in agreement with each other (Li et al. 2005; Hofmeister 2006; Zhang and Oganov 2006; Stackhouse et al. 2007a; Bengtson et al. 2008, 2009; Umemoto et al. 2008, 2009; Hsu et al. 2009b). The HS-to-LS crossover pressure in ferrous iron in $(Mg,Fe)SiO_3$ determined by static calculations strongly depends on the choice of exchange-correlation functional among other things. In general, GGA gives higher transition pressure than LDA by ~50 GPa (Hofmeister 2006; Zhang and Oganov 2006; Stackhouse et al. 2007; Bengtson et al. 2008; Umemoto et al. 2008; Hsu et al. 2009b), as has been seen in other non-strongly-correlated systems as well (Tsuchiya et al. 2004; Yu et al. 2007, 2008, Wentzcovitch et al. 2010). It also depends on other factors, such as the magnetic and atomic order (Umemoto et al. 2008), the site degeneracy of irons (Umemoto et al. 2009), and the inclusion of on-site Coulomb interaction, Hubbard U (Hsu et al. 2009b). In all these calculations, the HS-to-IS transition was not observed. The spin-state transition of ferric iron is also discussed in some theoretical works (Li et al. 2005; Zhang and Oganov 2006; Stackhouse et al. 2007). The results of these calculations are summarized (with selected iron concentrations x) in Table 2. Since ferrous iron has greater population in perovskite and it occupies the A site, our work (Umemoto et al. 2008, 2009; Hsu et al. 2009b) have focused on Al-free iron-bearing

Table 2. Computed HS-to-LS transition pressures of Fe^{3+} and Fe^{2+}. There are two transition pressures adopted from Umemoto et al. (2008) for each method. The higher transition pressure corresponds to the configuration with uniformly distributed iron cations, and the iron-(110) configuration (see text) gives the lower transition pressure shown in table.

Composition	*x*	Method	Iron	HS-to-LS	Reference
$(Mg,Fe)(Si,Al)O_3$	0.0625	GGA	Fe^{3+}	105 GPa	Li et al. 2005
$(Mg,Fe)(Si,Al)O_3$	0.03125	GGA	Fe^{3+}	134 GPa	Zhang & Oganov 2006
$(Mg,Fe)(Si,Fe)O_3$	0.0625	GGA	Fe^{3+} (A site)	76 Gpa	Zhang & Oganov 2006
$(Mg,Fe)(Si,Fe)O_3$	0.125	GGA	Fe^{3+} (A site)	60 GPa	Stackhouse et al. 2007
$(Mg,Fe)SiO_3$	0.125	GGA	Fe^{2+}	130 GPa	Stackhouse et al. 2007
$(Mg,Fe)SiO_3$	0.125	GGA	Fe^{2+}	202 GPa	Bengtson et al. 2008
$(Mg,Fe)SiO_3$	0.25	LDA	Fe^{2+}	96 GPa	Bengtson et al. 2008
$(Mg,Fe)SiO_3$	0.125	LDA	Fe^{2+}	56-97 GPa	Umemoto et al. 2008
$(Mg,Fe)SiO_3$	0.125	GGA	Fe^{2+}	117-160 GPa	Umemoto et al. 2008
$(Mg,Fe)SiO_3$	0.125	LDA+*U*	Fe^{2+}	~ 300 GPa	Hsu et al. 2009b
$(Mg,Fe)SiO_3$	0.125	GGA+*U*	Fe^{2+}	> 300 GPa	Hsu et al. 2009b

perovskite, namely, $(Mg_{1-x}Fe_x)SiO_3$. The results of these calculations are discussed below. In the lower mantle $x \approx 0.1$, and we set $x = 0.125$ in our calculations.

Quadrupole splitting of ferrous iron in perovskite

The stability of IS iron and its QS is the first issue we address. The QS is directly proportional to the product of the nuclear quadrupole moment and the electric field gradient (EFG) at the center of iron nucleus. The EFG depends on the asymmetry of the charge density around the nucleus and is not determined solely by the spin state. In $(Mg,Fe)SiO_3$ perovskite, ferrous iron substitutes for magnesium in the large 8-12 coordinated cage. This is a large cage and iron might find metastable sites, in addition to the lowest energy site. The ligand field, the *d*-orbital occupancy, and the electron charge distribution might differ among these sites. Such difference, even if small, can change the EFG and thus lead to different QSs, irrespective of spin state. Therefore, interpretation of the spin state on the basis of QSs observed by Mössbauer spectroscopy is not unambiguous.

Bengtson et al. (2009) conducted a random search for possible equilibrium HS iron sites by displacing them from their "previously known" equilibrium position and subsequently relaxing them. This GGA investigation found two metastable sites for HS iron in $(Mg_{0.75}Fe_{0.25})SiO_3$. Their QSs were 3.2 and 2.3 mm/s. At 0 GPa, the site with small QS was 8 meV/Fe more stable than the HS QS site. The atomic configurations of these two sites around iron at 0 GPa are shown in Figure 14 (Bengtson et al. 2009). They produce different ligand fields. No other metastable site was found for HS iron. While the energy difference between these HS states was noticed to decrease with pressure, the enthalpy crossing between them was not demonstrated (Bengtson et al. 2009). They also indicated that the QS of (the manually constrained) IS iron was 0.7 mm/s, far smaller than the 3.5-4.0 mm/s observed by McCammon et al. (2008). The QS for the LS state calculated by Bengtson et al. (2009) was 0.8 mm/s.

A systematic search for metastable equilibrium sites of iron in $MgSiO_3$ perovskite in HS, LS, and IS states was conducted by Hsu et al. (2009b). These calculations started searching for unstable phonons (GGA) in a cubic perovskite structure with 20 atoms supercell. The

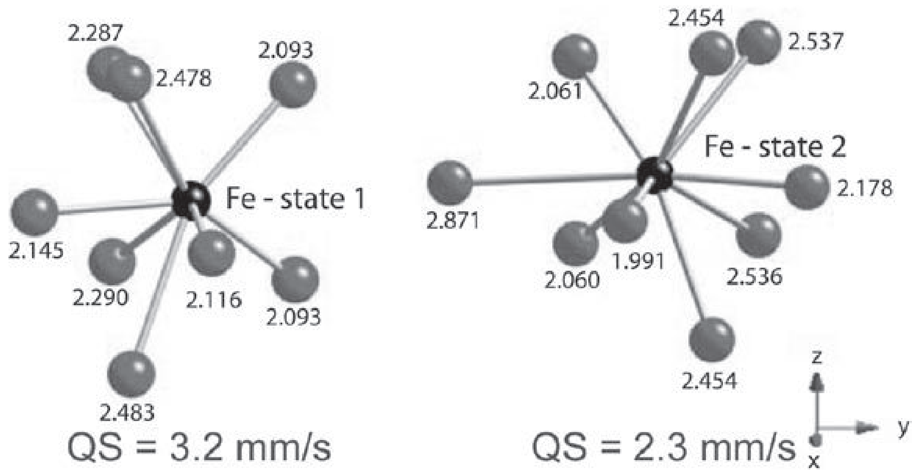

Figure 14. Local atomic configurations around two HS iron with different quadrupole splittings in $(Mg_{0.75}Fe_{0.25})SiO_3$ perovskite at zero pressure. The state with QS = 2.3 mm/s has lower energy than the state with QS = 3.3 mm/s by 0.8 meV/Fe at zero pressure. [Used by permission of AGU, from Bengtson et al. (2009)].

displacement modes of the unstable phonons were subsequently added to the atomic positions followed by full structural relaxations. Phonon frequencies were recalculated and this process was repeated until no more unstable phonons were present. Three HS and three LS sites were found in $(Mg_{0.75}Fe_{0.25})SiO_3$. It turned out that only the HS states with QS of 2.3 and 3.3 mm/s and the LS state with QS 0.8 mm/s are in the relevant energy range, with the two relevant HS states are competing energetically with each other. The local relevant atomic configurations of HS iron found in this work are similar to those shown in Figure 14 (Bengtson et al. 2009). At 0 GPa, the low-QS (2.3 mm/s) HS structure has slightly larger volume, and its energy is lower than that of the high-QS (3.3 mm/s) state by 24.3 meV/Fe. The high-QS HS structure is the same HS structure obtained by Umemoto et al. (2008, 2009). A stable IS state with QS of 1.4 mm/s is found in Hsu et al. (2009b). This IS state is the same as that obtained in Umemoto et al. (2009). In the 30-150 GPa pressure range, the magnetic moment of this state converged spontaneously to $2\mu_B$ ($S = 1$). This QS value, although higher than that obtained in Bengtson et al. (2009), is still considerably lower than 3.5-4.0 mm/s measured by MaCammon et al. (2008).

The reason why the QSs of the two competing HS states differ was discussed in Hsu et al. (2009b). The QS value depends on the EFG at the center of the iron nucleus, and the EFG is produced by the electron density. For both HS states, the spin-up electrons fill all five *d*-orbitals. Their contribution to the EFG is negligible since their charge density is essentially spherical. The EFG thus results primarily from the spin-down electron density. The major component of the EFG tensor, V_{zz}, depends on the orbital occupancy according to:

$$V_{zz} \propto \frac{e}{r^3}\left(2n_{xy} - n_{yz} - n_{xz} - 2n_{z^2} + 2n_{x^2-y^2}\right)$$

where n_{xy}, n_{yz},… correspond to the occupancy of the d_{xy}, d_{yz}, …, orbitals respectively (Chen and Yang 2007). Electrons occupying d_{xy}, $d_{x^2-y^2}$, or d_{z^2} orbitals contribute twice as much to the EFG as those in d_{xz} or d_{yz} orbitals. In the high-QS HS state, the spin-down occupancies are ~0.47 and ~0.62 for the $d_{x^2-y^2}$ and d_{xy} orbitals, respectively, and essentially 0.0 for the other orbitals. In the low-QS HS structure, only the d_{yz} orbital has significant occupancy, ~0.97. This difference in *d*-orbital occupancies of the HS states is the origin of their different QSs.

The effect of X_{Fe}, exchange-correlation functional (GGA, LDA), and Hubbard U on the low-to-high QS and spin-state crossover was also investigated by Hsu et al. (2009). The

Hubbard U was determined by the linear response of the corresponding DFT ground state to the local perturbation at the iron site (Cococcioni and de Gironcoli 2005). The pressure at which the enthalpies of the high- and low-QS HS states cross depends on all these factors. However, it always occurred below 24 GPa. The QSs increase with Hubbard U to 2.5 and 3.5 mm/s for the determined Us. The HS-to-IS enthalpy crossing was never observed between 0 and 150 GPa. The high enthalpy of IS was also demonstrated by Umemoto et al. (2009), as shall be discussed in the next sub-section.

Dependence of the spin crossover pressure on the site and orbital degeneracies

The spin-state crossover in $(Mg_{0.875}Fe_{0.125})SiO_3$ at finite temperatures is discussed in this sub-section (Umemoto et al. 2009). The effect of vibrations is disregarded, as in Tsuchiya et al. (2006), and only the effect of orbital and site degeneracies (Eqns. 7 and 8) are considered. The Gibbs free energy of each spin state (Eqn. 5) is then given by $G_\sigma = H_\sigma + G_\sigma^{mag} + G_\sigma^{site}$. The states involved are: the high-QS HS state, and the LS and IS relevant states. Only the high-QS HS state was relevant in this study (Umemoto et al. 2009) because this was an LDA calculation and the high- and low-QS HS states merged into a single one with high-QS at ~10 GPa (Hsu et al. 2009b), well before the HS-to-LS crossover occurs, ~100 GPa.

HS iron in perovskite is on a xy mirror plane, but the IS and LS are not. They are displaced from the xy mirror plane along the $\pm z$-axis, as shown in Figure 15. Therefore, there are two possible sites for IS and LS iron if irons are not close to each other. This means $N_{HS}^{site} = 1$, and $N_{IS}^{site} = N_{LS}^{site} = 2$ in Equation (8). The LDA enthalpy of IS iron is much higher than those of HS and LS iron, as shown in Figure 16 (Umemoto et al. 2009), and this makes the IS iron fraction n_{IS} negligible (< 3%) in 0-3000 K temperature range (Umemoto et al. 2009). The effect of site degeneracy on the LS iron fraction n_{LS} is demonstrated in Figure 17. To make this point clear the magnetic entropy was temporarily disregarded. Site entropy does not affect n_{LS} at 0 K, as expected. At finite temperatures, it helps to stabilize the LS state with respect to the HS state. Without site entropy, the HS-to-LS crossover pressure (at which $n_{LS} = 0.5$) is 97 GPa at all temperatures. With site entropy, the crossover pressure changes to 95, 88, 80, and 72 GPa at the temperature of 300, 100, 2000, and 3000 K, respectively. Therefore, at lower-mantel temperatures, site entropy should decrease noticeably the onset of the spin-state crossover. It should be noted that this calculation is based on the assumption of ideal solid solution with uniformly distributed irons. For higher iron concentrations or other atomic configurations where iron-iron interactions are not negligible (Umemoto et al. 2008), this effect is probably smaller.

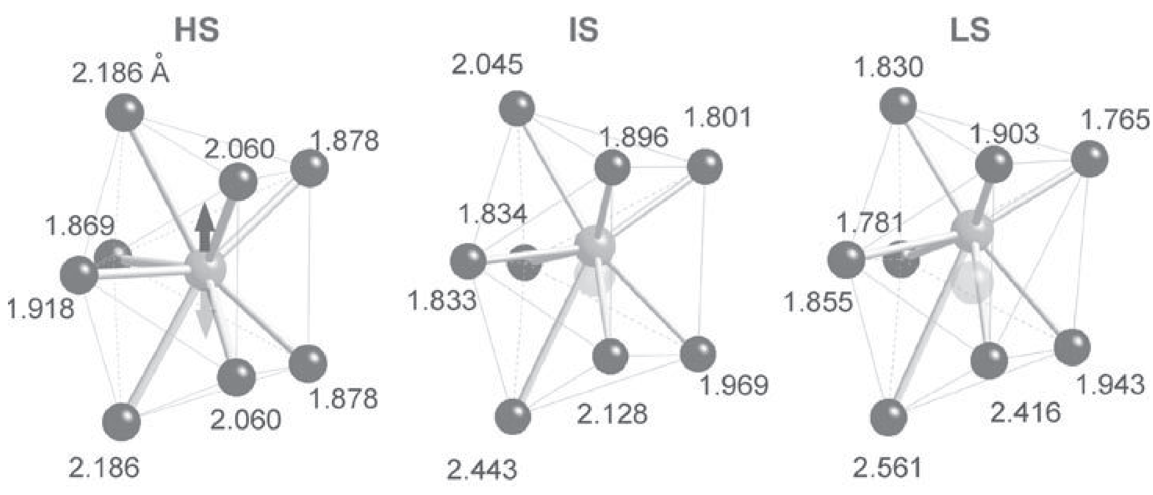

Figure 15. Local atomic configurations around HS, IS, and LS iron at 120 GPa optimized for $(Mg_{0.875}Fe_{0.125})SiO_3$ with LDA. Numbers next to oxygens are Fe-O distances (in Å). Pale spheres represent symmetrically equivalent sites for IS and LS states. [Used by permission of Elsevier, from Umemoto et al. (2009)].

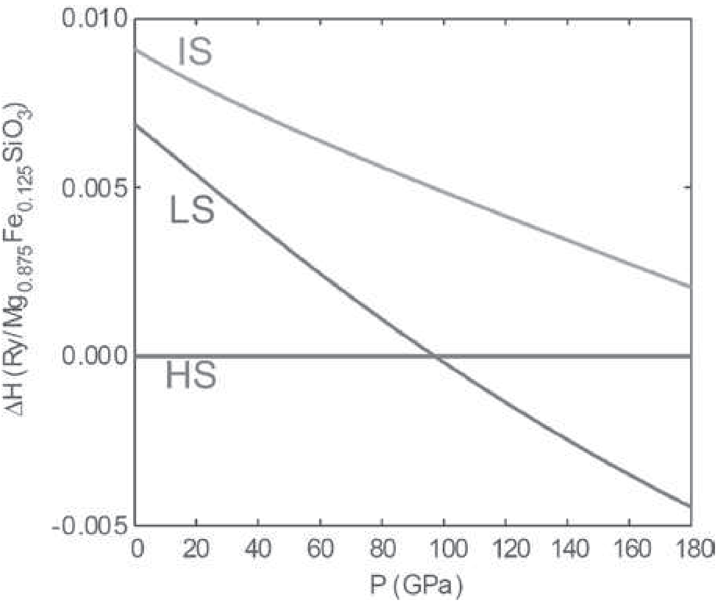

Figure 16. Relative enthalpies of the LS and IS with respect to the HS $(Mg_{0.875}Fe_{0.125})SiO_3$. The calculation was performed using LDA. [Used by permission of Elsevier, from Umemoto et al. (2009)].

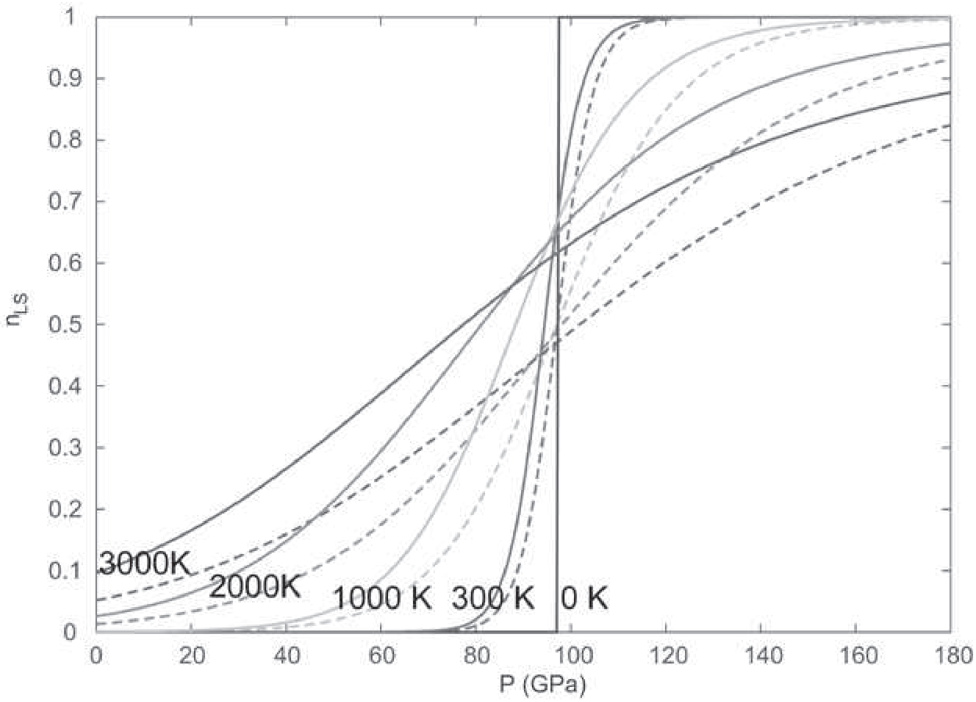

Figure 17. LS iron fraction (n_{LS}) at several temperatures. Solid and dashed lines denote n_{LS} calculated with and without LS site entropy, respectively. Magnetic entropy is disregarded in this figure. [Used by permission of Elsevier, from Umemoto et al. (2009)].

Inclusion of the magnetic entropy term in the free energy introduces a different temperature dependence in the crossover pressure. The spin quantum numbers and orbital degeneracies (Eqn. 7) are: $S_{LS} = 0$, $S_{IS} = 1$, $S_{HS} = 2$, and $m_{LS} = m_{IS} = m_{HS} = 1$. Figure 18 shows the $n_{LS}(P,T)$ with magnetic entropies. Since the term $m_{HS}\,(2S_{HS}+1) > N_{LS}^{site}$, the magnetic entropy has greater effects than the site entropy. However, comparison between Figures 18(a) and 18(b) show that the effect of site entropy can still be observed. Site entropy expands the stability field of the LS state, partially compensating the effect of magnetic entropy, which favors the HS state.

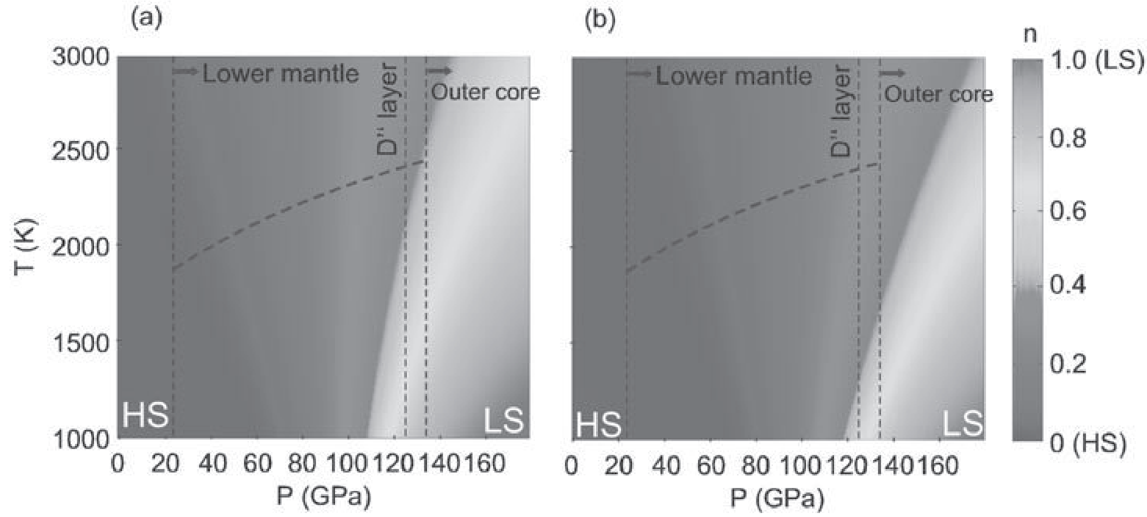

Figure 18. LS iron fraction (n_{LS}) with magnetic entropy. In (a) the LS site entropy is included, while in (b) it is not. Dashed lines denote a mantle geotherm derived by Brown and Shankland (1981). [Used by permission of Elsevier, from Umemoto et al. (2009)].

The compression curves and the bulk modulus of $(Mg_{0.875}Fe_{0.125})SiO_3$ in pure and mixed-spin states are shown in Figures 19 and 20, respectively. While the calculated volumes at 300 K (271.55 a.u.^{3}/f.u), are underestimated in LDA calculations (experimental value 275.50 a.u.^{3}/f.u.) owing to the absence of vibrational zero point motion effects in this calculation, the bulk modulus reproduces the experimental value 257 GPa (Lundin et al. 2008) quite well. The volume difference between the LS and HS states is quite small (about 0.3%). Therefore, even at 300 K, the volume reduction accompanying the spin-state crossover is difficult to observe, let alone the case at 2000 K, as can be seen in Figure 19. This is very different from ferropericlase discussed earlier. In perovskite, the softening in bulk modulus "*for this particular atomic configuration*" is pronounced at 300 K but barely noticeable at 2000 K, as shown in Figure 20. Therefore, at lower-mantle conditions, the elastic properties of perovskite should be in practice unaffected by the spin-state crossover.

Dependence of transition pressure on the concentration and distribution of iron

Our discussions so far have been focused on the calculations with low concentration (X_{Fe} = 0.125) of iron distributed uniformly in the perovskite. Iron-iron interaction is weak in this case and the ideal solid solution approximation is fine for sake of understanding different effects. However, iron-iron interaction is non-negligible at higher iron concentrations or for low iron concentration in clustered iron configurations. A thorough study with a variety of spatial distributions of irons at various concentrations ($0.0625 \le X_{Fe} \le 1.0$) was conducted by Umemoto et al. (2008). Two extreme configurations at X_{Fe} = 0.125 and 0.5 are shown in Figure 21: one configuration with uniformly distributed irons and the other with irons ordered in the (110) plane. The latter is referred to as iron-(110) hereafter. There can be ferromagnetic (FM) and anti-ferromagnetic (AFM) order in both configurations. The effect of magnetic order is not important. The HS-to-LS crossover pressure only differs by a few GPa (Umemoto et al. 2008). Therefore, we only mention results for the FM case.

Iron-iron interaction reduces the transition pressure. This interaction has a substantial elastic component. In either configuration, the transition pressure decreases with iron concentration, by about 100 GPa when X_{Fe} increases from 0.0625 to 1.0, as shown in Figure 22. In the range of $0.0625 \le X_{Fe} \le 0.125$, where iron-iron interactions are weak, the transition pressure is not sensitive to iron concentration for uniformly distributed configurations. For low

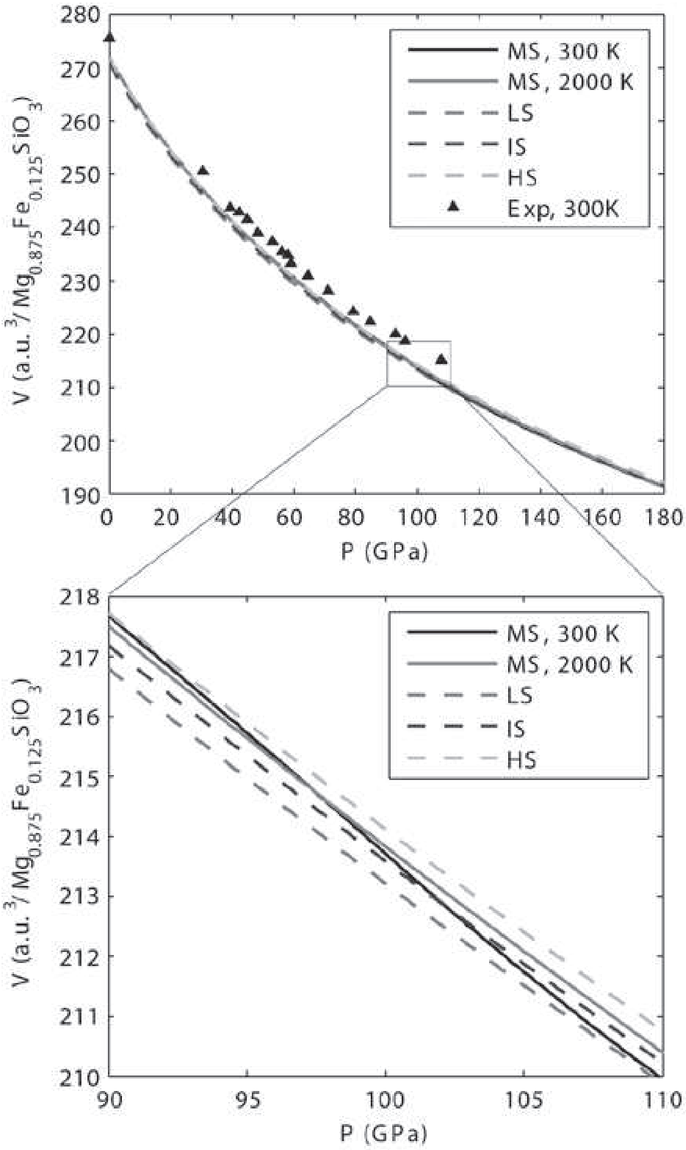

Figure 19. Compression curves for the MS state at 300 K and 200 K and for LS, IS, and HS state determined using LDA. It should be noted that vibrational contribution to the free energy is not included and volumes are underestimated. Experimental values for 15% iron concentration are taken from Lundin et al. (2008). [Used by permission of Elsevier, from Umemoto et al. (2009)].

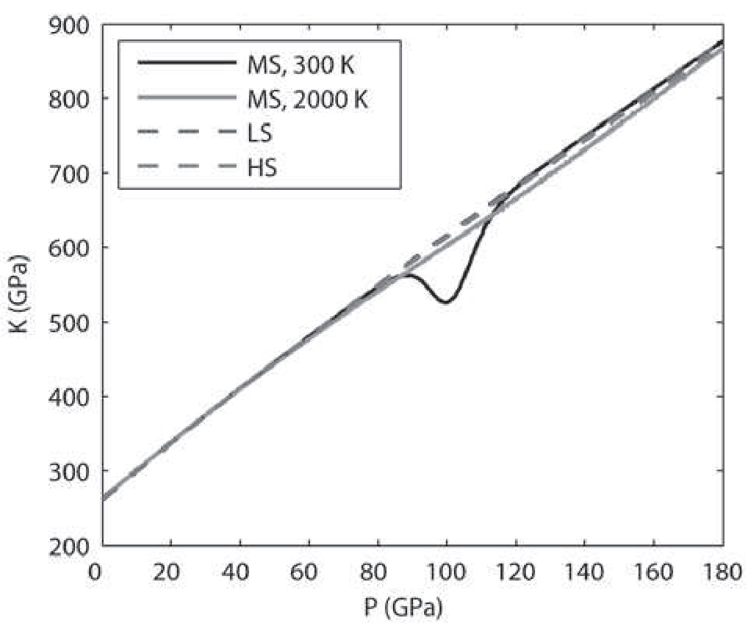

Figure 20. Pressure dependence of the calculated bulk modulus (LDA) of the MS state at 300 K and 2000 K and for the LS and HS states. [Used by permission of Elsevier, from Umemoto et al. (2009)].

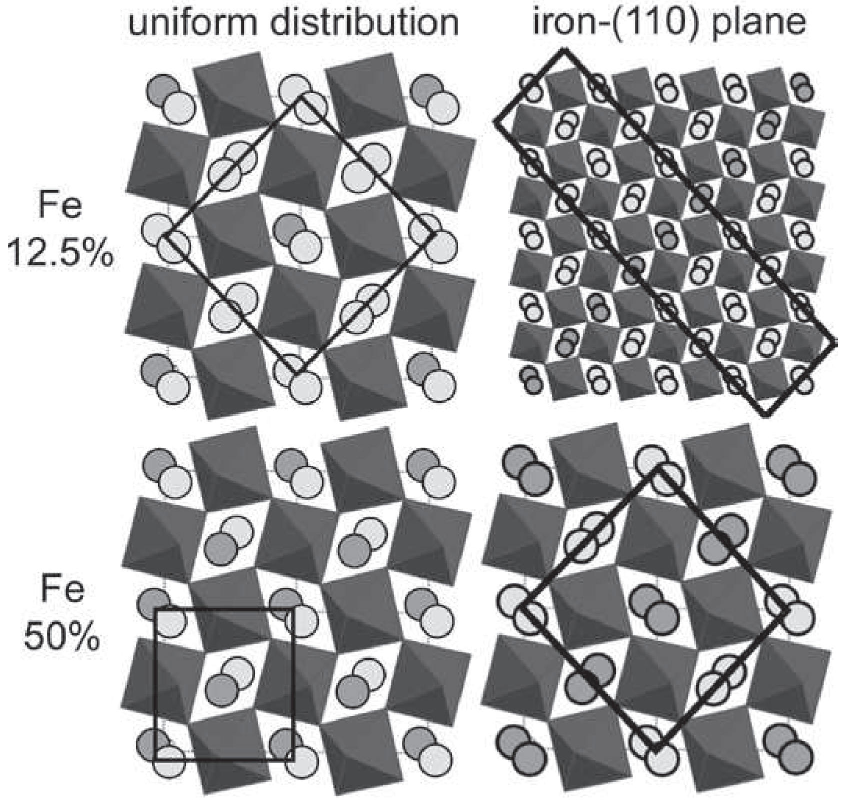

Figure 21. $(Mg_{0.5}Fe_{0.5})SiO_3$ and $(Mg_{0.875}Fe_{0.125})SiO_3$ in the configurations with iron distributed uniformly and iron placed on the (110) plane. [Used by permission of Elsevier, from Umemoto et al. (2008)].

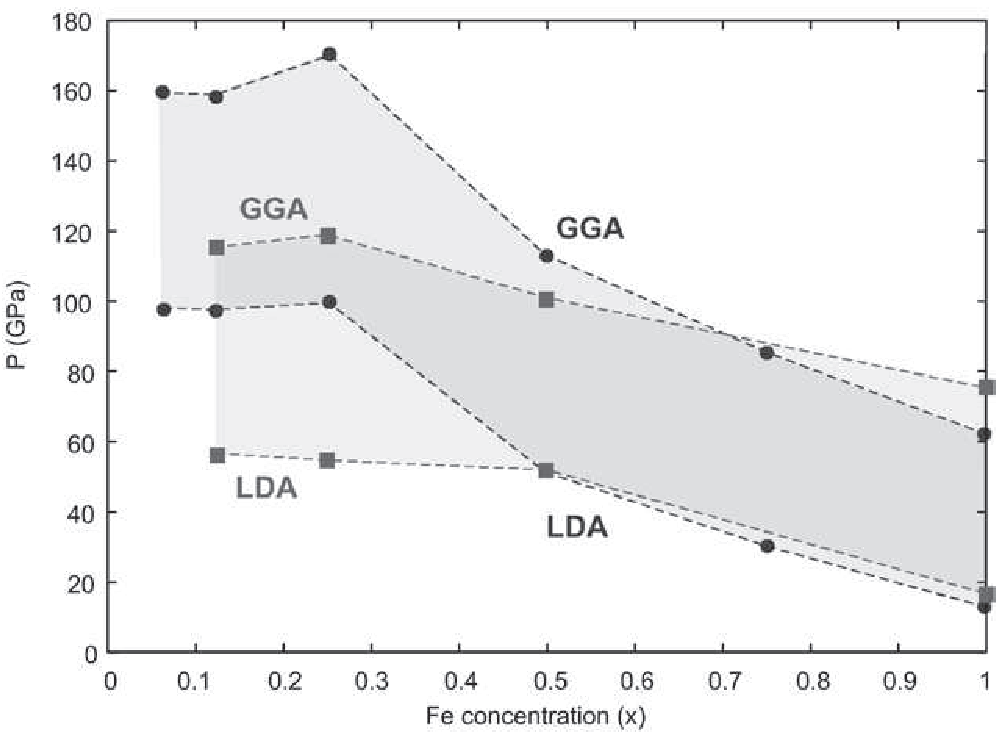

Figure 22. Calculated HS-to-LS transition pressure of $(Mg_{0.875}Fe_{0.125})SiO_3$ as a function of iron concentration in the case of iron distributed uniformly (circle) and the case of iron placed on the (110) plane (square). Both GGA and LDA are presented. Dashed lines and shaded bands are guides to the eye. [Used by permission of Elsevier, from Umemoto et al. (2008)].

iron concentration, the transition pressure in these two types of configurations differs by 50 GPa (Fig. 22). This effect is not important for $X_{Fe} \geq 0.5$ because irons are close and interacting to start with.

For both iron configurations with $X_{Fe} = 0.125$, the fraction of LS iron as a function of pressure and temperature are plotted in Figure 23. Vibrational effects are not present in this calculation. Only the orbital degeneracy (magnetic entropy) is included. It can be expected that the site degeneracies have greater effect on the transition pressure in the iron-(110) configuration because there are more combinations of the iron displacement.

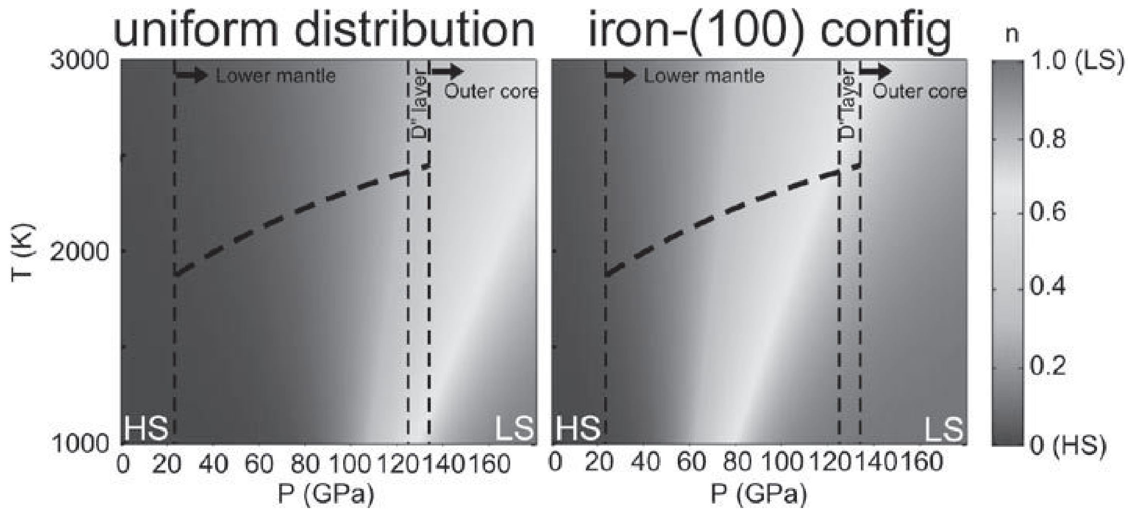

Figure 23. LS iron fraction (n_{LS}) of $(Mg_{0.875}Fe_{0.125})SiO_3$ in the case of iron distributed uniformly and the case of iron placed on the (110) plane. [Used by permission of Elsevier, from Umemoto et al. (2008)].

SPIN-STATE CROSSOVER IN POST-PEROVSKITE

The spin state and its crossover in iron-bearing $MgSiO_3$ post-perovskite are still very unclear. This is expected to be the major constituent of the D″ region, i.e, the region extending up to ~250 km above the core-mantle boundary (Murakami et al. 2004; Oganov and Ono 2004; Tsuchiya et al. 2004). Most of the experimental work on this phase was focused on the perovskite-to-post-perovskite transition in $MgSiO_3$ and the properties of $MgSiO_3$-post-perovskite, including estimations of the discontinuity in seismic wave speed produced by this transition (Garnero et al. 2004; Hernlund et al. 2005; Lay et al. 2006; van der Hilst et al. 2007; Wentzcovitch et al. 2006), elasticity (Merkel et al. 2006; Stackhouse and Brodholt 2007b; Wentzcovitch et al. 2006; Wookey et al. 2005), and thermal conductivity (Buffett 2007; Matyska and Yuen 2005a,b; Naliboff and Kellogg 2006). Synthesis (Mao et al. 2004), chemistry (Murakami et al. 2005), and Fe-Mg partitioning (Kobayashi et al. 2005) between $(Mg,Fe)SiO_3$-post-perovskite, perovskite, and ferropericlase have also been investigated. As to the valence- and spin-state of iron in $(Mg,Fe)SiO_3$-post-perovskite, there are very limited experimental works (Jackson et al. 2009; Lin et al. 2008) and they are not in agreement with each other. The experimental data presented in Lin et al. (2008) showed no ferric iron in the sample and ferrous iron appeared to be in the IS state at 134 GPa in the temperature range of 300-3200 K. However, ferric iron appears to be the dominant species in other experiments at 120 GPa and room temperature (Jackson et al. 2009).

First-principles GGA calculations agree that ferrous iron should remain in the HS state at least up to 150 GPa (Stackhouse et al. 2006; Zhang and Oganov 2006; Caracas and Cohen 2008), and IS should not be observed. As to ferric iron, it should also remain in the HS state

(Zhang and Oganov 2006). In summary, no spin-state crossover is observed in calculations, consistent with the experimental results by Jackson et al. (2009). However, the transition pressure should depend strongly on the exchange correlation functional and on the inclusion of on-site Coulomb interaction (Hubbard *U*). Clearly, much more needs to be investigated in this system to better understand this complex system.

SUMMARY

Results of several first-principles calculations on the spin-state crossover of iron in lower-mantle minerals have been reviewed. The LDA+*U* method gives desirable atomic and electronic structure in ferropericlase, (Mg,Fe)O. Both low-spin and high-spin ferropericlase are insulating. Jahn-Teller distortion is observed around iron in the high-spin state. A vibrational virtual crystal model (VVCM) permitted calculations of thermodynamic properties of this system at lower mantle conditions. Predictions are overall in good agreement with several experimental data sets. They display anomalies in the bulk modulus and allowed predictions of anomalies in thermodynamic properties and of the elastic signature of this phase in the mantle. An intriguing possibility of a viscosity anomaly caused by this crossover in the mantle has been raised. Improvements in these calculations to go beyond the ideal HS-LS solid solution are still desirable, as well as self-consistent calculations of the Hubbard *U*. These upgrades should improve agreement between predictions and measurements of crossover pressure ranges.

(Mg,Fe)SiO_3 perovskite is a more difficult system to investigate, therefore more controversial. Currently, there is lack of consensus regarding the existence of IS iron in perovskite. All calculations, irrespective of exchange-correlation functional used, agree on one issue: the IS state is not energetically competitive and no HS-to-IS crossover is expected to occur at lower-mantle pressures. The calculated HS-LS crossover pressure in ferrous iron strongly depends on the exchange-correlation functional (LDA, GGA, or DFT+*U*), and on the iron distribution in the supercell. This makes it more difficult to compare results with or interpret experimental data. A non-ideal HS-LS solid solution treatment appears to be essential for this system. On the positive side, the HS-LS crossover does not appear to affect the compressibility of this system to experimentally detectable levels. In the lower mantle, the change in compressibility of this system should be even less detectable. A thorough study of ferric iron using a more appropriate exchange-correlation functional or the DFT+*U* method is still needed for more extensive comparison between experimental data and theoretical results.

(Mg,Fe)SiO_3 post-perovskite is the least understood phase. Existing experimental data appear contradictory, and computational work is limited. The spin-state crossover in (Mg,Fe)SiO_3-post-perovskite is still a wide open question.

ACKNOWLEDGMENT

This research was supported by NSF grants EAR 0810272, EAR 0635990, ATM 0428774, EAR 0757903, and by the MRSEC Program of the National Science Foundation under Awards No. DMR-0212302 and No. DMR-0819885.

REFERENCES

Badro J, Fiquet G, Guyot F, Rueff JP, Struzhkin VV, Vanko G, Monaco G (2003) Iron partitioning in Earth's mantle: toward a deeo lower mantle discontinuity. Science 300:789-791

Badro J, Rueff JP, Vanko G, Monaco G, Fiquet G, Guyot F (2004) Electronic transitions in perovskite: possible nonconvecting layers in the lower mantle. Science 305:383-386

Badro J, Struzhkin VV, Shu J, Hemley RJ, Mao H, Kao C, Rueff J, Shen G (1999) Magnetism in FeO at megabar pressure from X-ray emission spectroscopy. Phys Rev Lett 83:4101-4104

Barnhoorn A, Bystricky M, Kunze K, Burlini L, Burg JP (2005) Strain localisation in bimineralic rocks: Experimental deformation of synthetic calcite-anhydrite aggregates. Earth Planet Sci Lett 240:748-763

Baroni S, de Gironcoli S, Dal Corso A, Giannozzi P (2001) Phonons and related crystal properties from density-functional perturbation theory. Rev Mod Phys 73:515-562

Bengtson A, Li J, Morgan D (2009) Mössbauer modeling to interpret the spin sate of iron in (Mg,Fe)SiO_3. Geophys Res Lett 36:L15301

Bengtson A, Persson K, Morgan D (2008) *Ab initio* study of the composition dependence of the pressure-induced spin crossover in perovskite (Mg_{1-x},Fe_x)SiO_3. Earth Planet Sci Lett 265:535-545

Blaha P, Schwarz K, Madsen GKH, Kvasnicka D, Luitz J (2001) *WIEN2k*, An Augmented Plane Wave + Local Orbitals Program for Calculating Crystal Properties (Karlheinz Schwarz, Techn. Universität Wien, Austria). ISBN 3-9501031-1-2

Boehler R (2000) High-pressure experiments and the phase diagram of lower mantle and core materials. Rev Geophys 38:221-245

Brown JM, Shankland TJ (1981) Thermodynamic parameters in the Earth as determined from seismic profiles. Geophys J R Astr Soc 66:579-596

Buffett BA (2007) A bound on her flow below a double crossing of the perovskite-post-perovskite phase transition. Geophys Res Lett 34:L17302

Caracas R, Cohen RE (2008) Ferrous iron in post-perovskite from first-principles calculations. Earth Planet Sci Lett 168:147-152

Carrier P, Justo JF, Wentzcovitch RM (2008) Quasiharmonic elastic constants corrected for deviatoric thermal stresses. Phys Rev V 78:144302

Ceperley DM, Alder BJ (1980) Ground state of the electron gas by a stochastic method. Phys Rev Lett 45:566-569

Chen YL, Yang DP (2007) Mössbauer Effect in Lattice Dynamics. Wiley-VCH, Weinheim

Cococcioni M (2010) Accurate and efficient calculations on strongly correlated minerals with the LDA+U method: review and perspectives. Rev Mineral Geochem 71:147-167

Cococcioni M, de Gironcoli S (2005) Linear response approach to the calculation of the effective interaction parameters in the LDA+*U* method. Phys Rev B 71:035105

Cohen RE, Mazin II, Isaak DG (1997) Magnetic collapse in transition metal oxides at high pressure: Implications for the Earth. Science 275:654-657

Crowhurst J, Brown JM, Goncharov A, Jacobsen SD (2008) Elasticity of (Mg,Fe)O through the spin transition of iron in the lower mantle. Science 319:451-453

Dziewonski AM, Anderson DL (1981) Preliminary references Earth model (PREM). Phys Earth Planet Interiors 25:297-356

Ekstrom G, Dziewonski AM (1998) The unique anisotropy of the Pacific upper mantle. Nature 394:168-172

Fabris S, de Gironcoli S, Baroni S, Vicario G, Balducci G (2005) Taming multiple valency with density functionals: A case study of defective ceria. Phys Rev B 71:041102

Fei Y, Zhang L, Corgne A, Watson H, Ricolleau A, Meng Y, Prakapenka V (2007) Spin transition and equation of state of (Mg,Fe)O solid solutions. Geophys Res Lett 34:L17307

Forte AM, Mitrovica JK (2001) Deep-mantle high-viscosity flow and thermochemical structure inferred from seismic and geodynamic data. Nature 410:1049-1056

Fyfe WS (1960) The possibility of d-electron uncoupling in olivine at high pressures. Geochim Cosmochim Acta 19:141-143

Gaffney ES, Anderson DL (1973) Effect of low-spin Fe^{2+} on the composition of the lower mantle. J Geophys Res 78:7005-7014

Garnero EJ, Maupin V, Lay T, Fouch M (2004) Variable azimuthal anisotropy in earth's lowermost mantle. Science 306:259-261

Gavriliuk AG, Lin JF, Lyubutin IS, Struzhkin VV (2006) Optimization of the conditions of synchrotron Mössbauer experiment for studying electron transition at high pressures by the example of (Mg,Fe)O magnesiowüstite. J Exp Theor Phys Lett 84:161-166

Giannozzi P, Baroni S, Bonini N, Calandra M, Car R, Cavazzoni C, Ceresoli D, Chiarotti GL, Cococcioni M, Dabo I, Dal Corso A, de Gironcoli S, Fabris S, Fratesi G, Gebauer R, Gerstmann U, Gougoussis C, Kokalj A, Lazzeri M, Martin-Samos L, Marzari N, Mauri F, Mazzarello R, Paolini S, Pasquarello A, Paulatto L, Sbraccia C, Scandolo S, Sclauzero G, Seitsonen AP, Smogunov A, Umari P, Wentzcovitch RM (2009) QUANTUM ESPRESSO: a modular and open-source software project for quantum simulations of materials. J Phys Condens Matter 21:395502

Goncharov AF, Struzhkin VV, Jacobsen SD (2006) Reduced radiative conductivity of low-spin (Mg,Fe)O in the lower mantle. Science 312:1205-1208

Grand SP, van der Hilst RD, Widyantoro S (1997) Global seismic tomography: A snapshot of convection in the earth. Geol Soc Am Today 7:1

Hernlund JW, Thomas C, Tackley PJ (2005) A doubling of the post-perovskite phase boundary and structure of the Earth's lowermost mantle. Nature 434:882-886

Hofmeister AM (2006) Is low-spin Fe^{2+} present in Earth's mantle? Earth Planet Sci Lett 243:44-52

Hohenberg P, Kohn W (1964) Inhomogeneous electron gas. Phys Rev 136:B864-871

Holtzman BK, Kohlstedt DL, Zimmerman ME, Heidelbach F, Hiraga T, Hustoft J (2003) Melt segregation and strain partitioning: Implications for seismic anisotropy and mantle flow. Science 301:1227-1230

Hsu H, Umemoto K, Cococcioni M, Wentzcovitch RM (2009a) First-principles study for low-spin $LaCoO_3$ with structurally consistent Hubbard *U*. Phys Rev B 79:125124

Hsu H, Umemoto K, Blaha P, Wentzcovitch EM (2009b) Spin states and hyperfine interactions of iron in $(Mg,Fe)SiO_3$ perovskite under pressure. Earth Planet Sci Lett (in review)

Jackson JM, Sturhahn W, Shen G, Zhao J, Hu MY, Errandonea D, Bass JD, Fei Y (2005) A synchrotron Mössbauer spectroscopy study of $(Mg,Fe)SiO_3$ perovskite up to 120 GPa. Am Mineral 90:199-205

Jackson JM, Sturhahn W, Tschauner O, Lerche M, Fei Y (2009) Behavior of iron in $(Mg,Fe)SiO_3$ post-perovskite assemblages at Mbat pressures. Geophys Res Lett 36:L10301

Kantor I, Dubrovinsky LS, McCammon CA (2006) Spin crossover in (Mg,Fe)O: A Mössbauer effect study with an alternative interpretation of X-ray emission spectroscopy data. Phys Rev B 73:100101(R)

Kantor I, Dubrovinsky LS, McCammon CA (2007) Reply to "Comment on 'Spin crossover in (Mg,Fe)O: A Mössbauer effect study with an alternative interpretation of X-ray emission spectroscopy data'". Phys Rev B 75:177103

Kantor I, Dubrovinsky LS, McCammon CA, Steinle-Neumann G, Kantor A (2009) Short-range order and Fe clustering in $Mg_{1-x}Fe_xO$ under pressure. Phys Rev B 80:014204

Keppler H, Kantor I, Dubrovinsky LS (2007) Optical absorption spectra of ferropericlase to 84 GPa. Am Mineral 92:433-436

Kobayashi Y, Kondo T, Ohtani E, Hirao N, Miyajima N, Yagi T, Nagase T, Kikegawa T (2005) Fe-Mg partitioning between $(Mg,Fe)SiO_3$ post-perovskite, perovskite, and magnesiowüstite in the Earth's lower mantle. Geophys Res Lett 32:L19301

Kohn W, Sham LJ (1965) Self-consistent equations including exchange and correlation effects. Phys Rev 140:A1133-1138

Kulik H, Cococcioni M, Scherlis DA, Marzari N (2006) Density functional theory in transition metal chemistry: A self-consistent Hubbard *U* approach. Phys Rev Lett 97:103001

Lay T, Hernlund J, Garnero EJ, Thorne M (2006) A post-perovskite lens and D″ hear flux beneth the central pacific. Science 314:1272-1276

Li J, Struzhkin V, Mao H, Shu J, Memeley R, Fei Y, Mysen B, Dera P, Pralapenka V, Shen G (2004) Electronic spin state of iron in lower mantle perovskite. Proc Nat Acad Sci USA 101:14027-14030

Li L, Brodholt JP, Stackhouse S, Weidner DJ, Alfredsson M, Price GD (2005) Electronic spin state of ferric iron in Al-bearing perovskite in the lower mantle. Geophys Res Lett 32:L17307

Lin JF, Gavriliuk AG, Struzhkin VV, Jacobsen SD, Sturhahn W, Hu M, Chow P, Yoo CS (2006a) Pressure-induced electronic spin transition of iron in magnesiowüstite-(Mg, Fe)O. Phys Rev B 73:113107

Lin JF, Gavriliuk AG, Sturhahn W, Jacobsen SD, Zhao J, Lerche M, Hu M (2009) Synchrotron Mössbauer spectroscopy of ferropericlase at high pressure and temperatures. Am Mineral 94:594-599

Lin JF, Jacobsen SD, Sturhahn W, Jackson JM, Zhao J, Yoo CS (2006b) Sound velocities of ferropericlase in Earth's lower mantle. Geophys Res Lett 33:L22304

Lin JF, Struzhkin VV, Gavriliuk AG, Lyubutin I (2007a) Comment on "Spin crossover in (Mg, Fe)O: A Mössbauer effect study with an alternative interpretation of X-ray emission spectroscopy data". Phys Rev B 75:177102

Lin JF, Struzhkin VV, Jaconsen SD, Hu MY, Chow P, Kung J, Liu H, Mao Hk, Hemley R (2005) Spin transition of iron in magnesiowüstite in the Earth's lower mantle. Nature 436:377-380

Lin JF, Tsuchiya T (2008) Spin transition of iron in the earth's lower mantle. Phys Earth Planet Inter 170:248-259

Lin JF, Vanko G, Jacobsen SD, Iota V, Struzhkin VV, Prakapenka VB, Kuznetsov A, Yoo CS (2007c) Spin transition zone in earth's lower mantle. Science 317:1740-1743

Lin JF, Watson H, Vanko G, Alp EE, Prakapenka VB, Dera P, Struzhkin V, Kubo A, Zhao J, McCammon C, Evans WJ (2008) Intermediate-spin ferrous iron in lowermost mantle post-perovskite and perovskite. Nature Geosci 1:688-691

Lin JF, Weir ST, Jackson DD, Evans WJ, Yoo CS (2007b) Electrical conductivity of the low-spin ferropericlase in the Earth's lower mantle. Geophys Res Lett 34:L16305

Lundin S, Catalli K, Santillan J, Shim SH, Prakapenka VB, Kunz M, Meng Y (2008) Effect of Fe on the equation of state of mantle silicate perovskite over 1 Mbar. Phys Earth Planet Inter 168:97-102

Madsen G, Blaha P, Schwarz K, Sjoestedt E, Nordstroem L (2001) Efficient linearization of the augmented plane-wave method. Phys Rev B 64:195134

Mao WL, Shen G, Prakapenka VB, Meng Y, Campbell AJ, Heinz DL, Shu J, Hemley R, Mao H (2004) Ferromagnesian postperovekite silicates in the D″ layer of the Earth. Proc Nat Acad Sci USA 101:15867-15869

Matyska C, Yuen DA (2005a) The importance of radiative heat transfer on superlimes in the lower mantle with the new post-perovskite phase change. Earth Planet Sci Lett 234:71-81

Matyska C, Yuen DA (2005b) Lower mantle dynamics with the post-perovskite phase change, radiative thermal conductivity, temperature- and depth-dependent viscosity. Phys Earth Planet Inter 196-207

McCammon C, Kantor I, Narygina O, Rouquette J, Ponkratz U, Sergueev I, Mezouar M, Prakapenka V, Dubrovinsky L (2008) Stable intermediate-spin ferrous iron in lower-mantle perovskite. Nature Geosci 1:684-687

McDonough WF, Sun S (1995) The composition of Earth. Chem Geol 120:223-253

Merkel S, Kubo A, Miyagi L, Speziale S, Duffy T, Mao H, Wenk H (2006) Plastic deformation of MgGeO3 post-perovskite at lower mantle pressures. Science 311:644-646

Mitrovica JK, Forte AM (2004) A new inference of mantle viscosity based on joint inversion of concecion and glacial isostatic adjustment data. Earth Planet Sci Lett 225:177-189

Murakami M, Hirose K, Kawamura K, Sata N, Ohishi Y (2004) Post-perovskite phase transition in $MgSiO_3$. Science 304:855-858

Murakami M, Hirose K, Sata N, Ohishi Y (2005) Post-perovskite phase transition and mineral chemistry in the pyrolitic lowermost mantle. Geophys Res Lett 32:L03304

Naliboff JB, Kellogg LH (2006) Dynamics effects of a step-wise increase in thermal conductivity and viscosity in the lowermost mantle. Geophys Res Lett 33:L12S09

Narygina O, Mattesini M, Kantor I, Pascarelli S, Wu X, Aquilanti G, McCammon C, Dubrovinsky L (2009) High-pressure experimental and computational XANES studies of (Mg,Fe)(Si,Al)O_3 perovskite and (Mg,Fe)O ferropericlase as in the Earth's lower mantle. Phys Rev B 79:174115

Nielsen OH, Martin RM (1983) First-principles calculations of stress. Phys Rev Lett 50:697-700

Oganov AR, Ono S (2004) Theoretical and experimental evidence for a post-perovskite phaseof $MgSiO_3$ in Earth's D″ layer. Nature 430:445-448

Ohnishi S (1978) A theory of pressure-induced high-spin-low-spin transition of transition metal oxides. Phys Earth Planet Inter 17:130-139

Pasternak MP, Taylor RD, Li X, Nguyen JH, McCammon CA (1997) High pressure collapse of magnetism in $Fe_{0.94}O$: Mössbauer spectroscopy beyond 100 GPa. Phys Rev Lett 79:5046-5049

Perdew JP, Burke K, Ernzerhof M (1996) Generalized gradient approximation made simple. Phys Rev Lett 77:3865-3868

Perdew JP, Ruzsinszky A (2010) Density functional theory of electronic structure: a short course for mineralogists and geophysicists. Rev Mineral Geochem 71:1-18

Perdew JP, Zunger A (1981) Self-interaction correction to density-functional approximations for many-electron systems. Phys Rev B 23:5048-5079

Persson K, Bengtson A, Ceder G, Morgan D (2006) *Ab initio* study of the composition dependence of the pressure-induced spin transition in the $(Mg_{1-x},Fe_x)O$ system. Geophys Res Lett 33:L16306

Petrilli HM, Blöchl PE, Blaha P, Schwarz K (1998) Electric-field-gradient calculations using the projector augmented wave method. Phys Rev B 57:14690-14697

Rappe AM, Rabe KM, Kaxrias E, Joannopoulos JD (1990) Optimized pseudopotentials. Phys Rev B 41:1227-1230

Ringwood AE (1982) Phase transformations and differentiation in subducted lithosphere: implications for mantle dynamics basalt petrogenesis and crustal evolution. J Geol 90:611-642

Sherman DM (1988) High-spin to low-spin transition of iron(II) oxides at high pressures: possible effects on the physics and chemistry of the lower mantle. *In*: Structural and Magnetic Phase Transition in Minerals. Ghose S, Coey JMD, Salje E (eds) Springer Verlag, New York, p 113-118

Sherman DM (1991) The high-pressure electronic structure of magnesiowüstite (Mg,Fe)O: applications to the physics and chemistry of the lower mantle. J Geophys Res 96(B9):14299-14312

Sherman DM, Jansen HJF (1995) First-principles predictions of the high-pressure phase transition and electronic structure of FeO: implications for the chemistry of the lower mantle and core. Geophys Res Lett 22:1001-1004

Speziale S, Lee VE, Clark SM, Lin JF, Pasternak MP, Jeanloz R (2007) Effects of Fe spin transition on the elasticity of (Mg,Fe)O magnesiowüstites and implications for the seismological properties of the Earth's lower mantle. J Geophys Res 112:B10212

Speziale S, Milner A, Lee VE, Clark SM, Pasternak M, Jeanloz R (2005) Iron spin transition on Earth's lower mantle. Proc Nat Acad Sci USA 102:17918-17922

Stackhouse S, Brodolt JP (2007b) The high-temperature elasticity of $MgSiO_3$ post-perovskite. *In*: Post-perovskite: The Last Mantle Phase Transition, Geophysical Monograph. Vol. 174. Hirose K, Brodholt J, Lay T, Yuen D (eds), American Geophysical Union, Washington DC, p 99-113

Stackhouse S, Brodolt JP, Dobson DP, Price GD (2006) Electronic spin transitions and the seimic properties of ferrous iron–bearing $MgSiO_3$ post-perovskite. Geophys Res Lett 33:L12S03

Stackhouse S, Brodolt JP, Price GD (2007a) Electronic spin transitions in iron-bearing $MgSiO_3$ perovskite. Earth Planet Sci Lett 253:282-290

Sugano S, Tanabe Y, Kamimura H (1970) Multiplets of Transition-Metal Ions in Crystals. Academic Press, New York and London

Touloukian YS, Kirdby RK, Taylor RE, Lee TYR (1997) Thermophysical Properties of Matter. Volume 13. Plenum Press, New York

Troullier N, Martines JL (1991) Efficient pseudopotentials for plane-wave calculations. Phys Rev B 43:1993-2006

Tsuchiya T, Tsuchiya J, Umemoto K, Wentzcovitch RM (2004) Phase transition in $MgSiO_3$ perovskite in the Earth's lower mantle. Earth Planet Sci Lett 224:241-248

Tsuchiya T, Wentzcovitch RM, da Silva CRS, de Gironcoli S (2006) Spin transition in magnesiowüstite in earth's lower mantle. Phys Rev Lett 96:198501

Umemoto K, Hsu H, Wentzcovitch RM (2009) Effect of site degeneracies on the spin crossover in $(Mg,Fe)SiO_3$ perovskite. Phys Earth Planet Inter (in press). doi: 10.1016/j.pepi.2009.10.014

Umemoto K, Wentzcovitch RM, Yu YG, Requist R (2008) Spin transition in $(Mg,Fe)SiO_3$ perovskite under pressure. Earth Planet Sci Lett 276:198-206

van der Hilst RD, de Hoop MV, Wang P, Shim SH, Ma P, Tenorio L (2007) Seismostratigraphy and thermal structure of earth's core-mantle boundary region. Science 315:1813-1817

van Westrenen W, Li J, Fei Y, Frank MR, Hellwig H, Komabayashi T, Mibe K, Minarik WG, van Orman JA, Watson HC, Funakoshi K, Schmidt W (2005) Thermoelastic properties of $(Mg_{0.64}Fe_{0.36})O$ ferropericlase based on in situ X-ray diffraction to 26.7 GPa and 2173 K. Phys Earth Planet Interiors 151:163-176

Vanderbilt D (1990) Soft self-consistent pseudopotentials in a generalized eigenvalue formalism. Phys Rev B 41:R7892-7895

Vanko G, de Groot FMF (2007) Comment on "Spin crossover in (Mg,Fe)O: A Mössbauer effect study with an alternative interpretation of X-ray emission spectroscopy data". Phys Rev B 75:177101

Wallace D (1972) Thermodynamics of Crystals. Wiley, New York

Wentzcovitch RM, Justo JF, Wu Z, da Silva CRS, Yuen DA, Kohlstedt D (2009) Anomalous compressibility of ferropericlase throughout the iron spin cross-over. Proc Nat Acad Sci USA 106:8447-8452

Wentzcovitch RM, Karki BB, Cococcioni M, de Gironcoli S (2004) Thermoelastic peroperties of MgSiO3-perovskite: Insights on the nature of the earth's lower mantle. Phys Rev Lett 92:018501

Wentzcovitch RM, Martins JL, Price GD (1993) Ab initio molecular dynamics with variable cell shape: application to MgSiO3. Phys Rev Lett 70:3947

Wentzcovitch RM, Tsuchiya T, Tsuchiya J (2006) $MgSiO_3$ postperovskite at D″ conditions. Proc Nat Acad Sci USA 103:543-546

Wentzcovitch RM, Yu YG, Wu Z (2010) Thermodynamic properties and phase relations in mantle minerals investigated by first principles quasiharmonic theory. Rev Mineral Geochem 71:59-98

Wookey J, Stackhouse S, Kendall JM, Brodholt JP, Price GD (2005) Efficacy of post-perovskite as an explanation for lowermost-mantle seismic properties. Nature 438:1003-1007

Wu Z, Justo JF, da Silva CRS, de Gironcoli S, Wentzcovitch RM (2009) Anomalous thermodynamic properties in ferropericlase throughout its spin crossover transition. Phys Rev B 80:014409

Yamazaki D, Karato S-i (2001) Some mineral physics constraints on the rheology and geotherm structure of Earth's lower mantle. Am Mineral 86:381-391

Yu Y, Wentzcovitch RM, Tsuchiya T (2007) First-principles investigation of the postpinel transition in Mg_2SiO_4. Geophys Res Lett 34:L10306

Yu Y, Wu Z, Wentzcovitch RM (2008) α-β-γ transformations in Mg_2SiO_4 in Earth's transition zone. Earth Planet Sci Lett 273:115-122

Zhang F, Oganov AR (2006) Valence state and spin transitions of iron in Earth's mantle silicates. Earth Planet Sci Lett 249:436-443

Zhao Y, Truhlar DG (2010) The Minnesota density functionals and their applications to problems in mineralogy and geochemistry. Rev Mineral Geochem 71:19-37